An Efficient Numerical Approach for Simulating Soil-Pipe Interaction Behaviour under Cyclic Loading

Miad Saberi [a], Charles-Darwin Annan [b], Brian B. Sheil [a]

[a] Department of Engineering Science, University of Oxford, Oxford, UK
[b] Department of Civil and Water Engineering, Université Laval, Québec, Canada

Corresponding Author: Miad Saberi, Ph.D., P.Eng.
Email: miad.saberi@eng.ox.ac.uk
miad.sabery@gmail.com

Abstract

Understanding soil-pipe interaction during cyclic axial displacement is essential for the design and evaluation of buried pipeline systems. This study introduces an efficient and practical numerical approach using beam-spring-interface elements to simulate soil-pipe interaction behaviour. Numerical predictions of the evolution of shear and normal stress distributions around the pipe are validated against full-scale experimental results for steel and high-density polyethylene pipes buried in sandy soils. Three different backfill cover depths and soil densities ranging between loose and dense were considered to allow a rigorous comparison between the numerical predictions and the experimental results. The results show that the proposed approach provides a high-fidelity representation of the complex soil-pipe interaction behaviour at the interface zones, including stress cyclic degradation, hardening and softening, cyclic accumulative contraction and stabilization. This numerical framework provides accurate predictions for a fraction of the computational cost of a full three-dimensional finite element analysis.

Keywords

Buried pipeline, soil-structure interface, soil-pipe interaction, cyclic axial loading, numerical modelling, experimental validation

1 Introduction

Buried pipelines are lifeline structures used for transporting critical utilities such as water, wastewater, oil and gas. The integrated response of the pipe to various loading conditions is highly dependent on interactions with the surrounding soil i.e. ‘soil-pipe interaction’ (SPI; Psyrras and Sextos 2018, Tsinidis et al. 2019). It is common for pipelines to experience axial displacements due to permanent ground movements (e.g. earthquake-induced, slope instability; Wijewickreme et al. 2009, Meidani et al. 2018) or cyclic excitation (e.g. changes in temperature of the transporting liquid, diurnal temperature fluctuations, and/or pipeline start-ups and shut-downs; Orourke and Hmadi 1988, Weidlich and Achmus 2008, Bilgin et al. 2012, Sheil et al. 2018, Castelo et al. 2019, Tian et al. 2021). Forces generated in the pipe walls due to these axial expansions/contractions can lead to global (e.g. upheaval) and local (e.g. wrinkling) buckling and fatigue damage. A thorough understanding of axial SPI therefore becomes a critical element towards achieving safe and economical pipeline design.

For offshore pipelines, it is common to lay the pipe directly on the seabed. In such cases, axial resistance is derived mainly from self-weight sliding of the pipe. Several studies have explored the role of pipeline ‘walking’ on pipeline stability and the development of axial pipe-seabed resistance (e.g. Carr et al. 2006, Bruton et al. 2010, White et al. 2011, Hill et al. 2012, Randolph 2012, Low et al. 2017, Reda et al. 2018, Guha et al. 2019, Castelo et al. 2019, Tian et al. 2021). Existing predictive methods for offshore pipelines have considered a range of simplified SPI behaviour including rigid plastic (Tian et al. 2021), elastic-perfectly plastic (Castelo et al. 2019), and velocity dependent rigid seabed (Guha et al. 2019). More advanced time-dependent behaviour models based on critical state soil mechanics (CSSM) were developed by Randolph et al. (2012) and Low et al. (2017) to predict peak and residual axial soil resistances throughout the operational life.

In contrast, onshore pipelines are commonly buried for mechanical protection from above-ground activities. For shallow embedment depths, normal contact stresses at the pipe crown and springline can be significantly lower than those at the invert due to the combined weight of the pipe and transported medium. This leads to a range of complex SPI phenomena such as volumetric compaction and dilation, shear stress hardening and softening under axial monotonic loading (Karimian 2006, Wijewickreme et al. 2009, Sarvanis et al. 2018, Al-Khazaali and Vanapalli 2018), normal and shear contact stress degradation, stress stabilization and accumulative contraction under cyclic loading (Weidlich and Achmus 2008, Bilgin et al. 2009, Huber and Wijewickreme 2014, Sheil et al. 2018, 2021). Cyclic axial loading of pipes buried in granular soils may also cause particle breakage, which can significantly affect the circumferential distribution of normal contact stress acting on the pipe. These phenomena result in important differences in the analysis of buried and on-the-bottom pipeline systems such that existing design methods for offshore pipelines cannot be reliably applied to buried pipelines.

The most common design approach for axial soil resistance in granular soils is defined in ALA (2001, 2005):

$$\sigma_n = 0.5\gamma' H(1 + K_0) \quad \text{1a}$$

$$F = (\pi D)\sigma_n \, tan\, \delta \quad \text{1b}$$

where σ_n is the average effective normal stress acting on the pipe, F is the axial soil resistance per unit length, γ' is the average effective unit weight of the backfill soil, H is the cover depth measured to the pipe springline, K_0 is the coefficient of lateral earth pressure at rest for the soil, δ is the soil-pipe interface friction angle, and D is the external pipe diameter. In this study, all stresses are considered as effective. Alternative modeling techniques such as the beam-on-nonlinear Winkler foundation (BNWF), the shell-on-Winkler foundation, and the hybrid beam-shell model have been proposed in the literature. These simplified methods are incapable of addressing the complex SPI phenomena occurring in buried pipe systems. Although 3-D continuum modelling can capture advanced SPI, the high computational cost and the need for advanced constitutive models limit its applicability for routine design practice (e.g. Vazouras et al. 2010, 2015, Rajeev and Kodikara 2011, Saberi et al. 2015, Sarvanis et al. 2018, Psyrras et al. 2019, Tsinidis et al. 2020, Elshesheny et al. 2020).

There remains an unmet need for a computationally efficient numerical modelling procedure capable of capturing these advanced SPI behaviours for buried pipelines. To address this shortcoming, this study describes the development of a new ‘Hybrid Winkler Interface’ (HWI) approach in which beam elements are used to simulate the behaviour of the pipe and a family of soil springs in different directions are used to simulate the effect of the surrounding soil. Thin-layer interface elements are employed to capture advanced SPI effects. The proposed model is validated through comparisons with experimental results published elsewhere in the literature.

2 Research Background: Buried Pipelines

Many experimental studies have explored pipeline response to vertical loading (e.g. Mir Mohammad Hosseini and Moghaddas Tafreshi 2002, Di Prisco and Galli 2006, Talesnick et al. 2011, Ahmed et al. 2015, Elshesheny et al. 2019a, 2019b), lateral loading (e.g. Brennodden et al. 1986, Calvetti et al. 2004, Cheuk et al. 2007, Minh and Zhang 2019, Ansari et al. 2019), combined vertical-lateral loading (e.g. Zhang et al. 2001, 2002, Tian et al. 2010), oblique axial-lateral loading (e.g. Daiyan et al. 2011), and axial displacement under monotonic (e.g. Scarpelli et al. 2003, Anderson et al. 2004, Karimian 2006, Wijewickreme et al. 2009, Sarvanis et al. 2018, Al-Khazaali and Vanapalli 2018) and cyclic conditions (Weidlich and Achmus 2008, Bilgin et al. 2009, 2012, White et al. 2011, Huber and Wijewickreme 2014, Sheil et al. 2018, 2021). ALA (2001) is a widely used design guideline and defines four main contributions of soil restraint on a buried pipe, namely (a) axial, (b) vertical-uplift, (c) vertical-bearing and (d) lateral. Relative soil-pipe axial displacement has been shown to induce volumetric deformations in the adjacent soil and causes significant changes to the normal stress distribution acting on the pipe (Weidlich and Achmus 2008, Wijewickreme et al. 2009, Meidani et al. 2017, Sheil et al. 2021).

A plethora of numerical approaches have been proposed for SPI analysis. A popular technique is the ‘beam-on-nonlinear Winkler foundation’ (BNWF) wherein the pipe is represented by beam elements and the surrounding soil is simulated using four sets of discrete springs as shown in Figure 1-a. While this methodology is simple, computationally efficient, and features frequently in the literature (e.g. Takada and Tanabe 1987, Lee et al. 2009, Saberi et al. 2011a, 2011b), it cannot capture certain pipe damage modes such as local buckling and ovalization. For this reason, the pipe has also been modelled using shell elements in the literature, as shown in Figure 1-b (e.g. Yang et al. 1988, Xie et al. 2013, Dadfar et al. 2015). To improve computational efficiency, this approach was later modified such that only the critical section of the buried pipe under study is represented by shell elements while the rest of the pipe is represented by beam elements i.e. a ‘hybrid shell-beam model’ (see Figure 1-c; e.g. Saberi et al. 2013). A key drawback of these approaches is the use of overly simplified soil springs which fail to capture realistic SPI effects and often introduce spurious local forces at spring-pipe connection points (Tsinidis et al. 2019). In this case, the boundary nodes on the pipe (shell) circumference are connected to the starting node of the beam element using a coupling

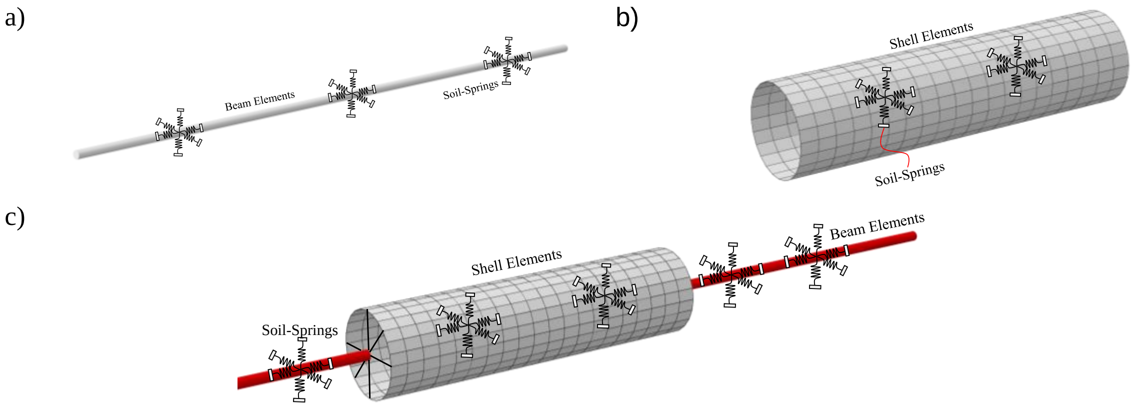

Figure 1. Soil-pipe interaction modelling approaches; a) Beam-on-nonlinear-Winkler-foundation, b) Shell on Winkler foundation, and C) Hybrid beam-shell model.

constraint. Other modelling approaches have been proposed for evaluating upheaval buckling using the beam element theory by Palmer et al. (1990) and DNV-RP-F11 (Det Norske Veritas 2007) for buried pipes commonly in the offshore industry.

3 Experimental Evidence

Results from three different full-scale experimental programmes on pipes buried in sandy soils are used to validate the proposed HWI model. The experiments considered steel pipes with different burial depths (Sheil et al. 2018), and high density polyethylene (HDPE) pipes in sands with different relative densities (Weidlich and Achmus 2008, Bilgin et al. 2009, 2012).

3.1 Case Study A: Steel Pipe in Sand (Sheil et al. 2018)

The full-scale testing apparatus described in Sheil et al. (2018, 2021) is shown schematically in Figure 2. The test pipe was machined from steel with an outside diameter of $D = 0.35$ m, wall thickness of 6 mm and surface roughness $R_{\max} = 39.2$ μm (relative roughness of 0.11 categorised as intermediate to rough; Dietz 2000, Hu and Pu 2004) and had an effective weight of 4 kN/m. The pipe was instrumented for measurement of the axial resistance developed on an isolated epoxy-coated central section. The central section was also fitted with three degree-of-freedom (DOF) load cells to measure the normal and shear contact stresses at six circumferential

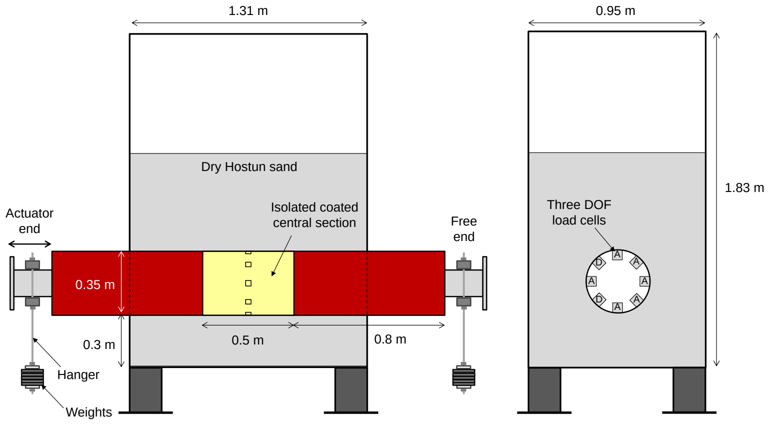

Figure 2. Front and side views of test set-up showing instrumented test pipe installed in a tank

Table 1 Properties of sandy soils used in laboratory tests

Property	**Hostun sand (Sheil et al. 2018)**	**Quartz sand (Weidlich and Achmus 2006, 2008)**	**Sand (Bilgin et al. 2009)**
Mean grain size, D_{50} (mm)	0.35	0.35	0.6
Relative density, D_r (%)	35	40, 50, 70	-
Min. void ratio, e_{min}	0.58	0.49	-
Max. void ratio, e_{max}	0.99	0.79	-
Initial void ratio, e_{in}	0.847	0.67, 0.64, 0.58	0.52
Coefficient of uniformity, C_u	1.4	2.21	2.6
Specific gravity, G_s (g/cm^3)	2.65	2.63	~2.65
Effective unit weight, γ' (kN/m3)	13.7	-	17.0
Peak friction angle, ϕ'_{peak} (deg)	37.9	-	-
Critical state friction angle, ϕ'_{cs} (deg)	35.4	38	~38

locations, as shown in Figure 2. The testing tank measured 0.95 m wide, 1.31 m long and 1.83 m high.of dry Hostun sand (A = active load cell, D = dummy load cell).

The tests made use of dry Hostun HN31 sand, the properties of which are listed in Table 1 (Colliat et al. 1986, Flavigny et al. 1990, Sheil et al. 2018). Measurements of the peak and critical state friction angles were obtained from triaxial tests on samples with a relative density of 51% and at a confining pressure of 80 kPa. Each sample was prepared by 'raining' the sand into the testing tank; in situ density pot measurements revealed an average relative density, D_r, of 35% ± 2% and an initial void ratio e_{in} of 0.847 at the level of the pipe springline.

Experimental results derived from three different 'test scenarios', representing different trench condition and degrees of overburden confinement, are used to rigorously validate the present numerical approach (see Figure 3):

(a) scenario I – overburden fully replicated with 0.5 m soil cover (measured from the pipe crown);

(b) scenario II – overburden fully replicated with 1·0 m soil cover;

(c) scenario III – overburden replicated with 1.1 m of soil cover in conjunction with a pressure bag system overlying an 18 mm thick plywood platen.

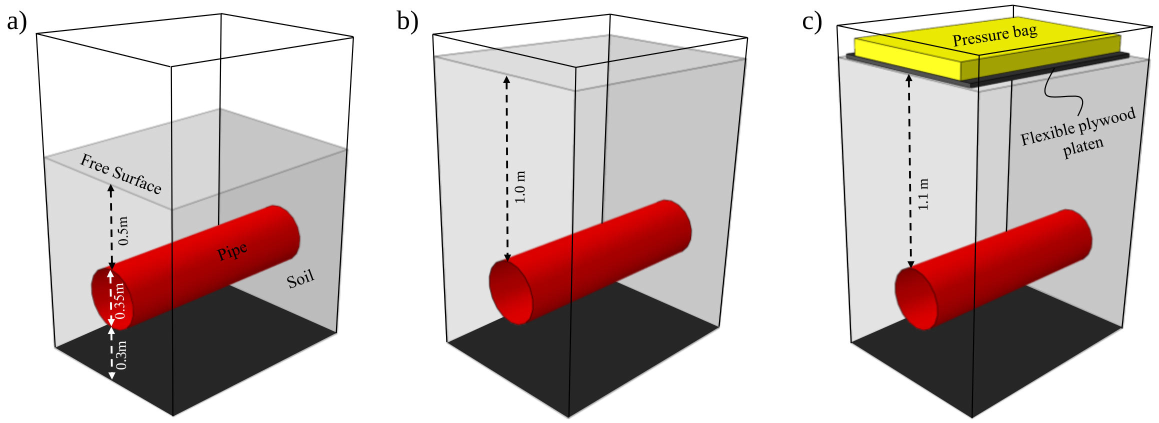

Figure 3. Schematic of soil-pipe interaction testing scenarios, a) scenario I, b) scenario II, and c) scenario III

For scenario III, the nominal overburden pressure, σ_v, acting at the level of the pipe crown was determined as:

$$\sigma_v = \gamma' h + p_{bag} A_r \qquad 2$$

where h is the depth of soil cover measured from the pipe crown, p_{bag} = 54 kPa is the bag pressure and A_r = 0.64 is the pressure bag area ratio (bag plan area divided by tank plan area; Sheil et al. 2018). The nominal σ_v at the pipe crown was therefore 6.9 kPa, 13.7 kPa and 50 kPa for scenarios I, II and III respectively.

Each test involved the application of displacement-controlled axial pipe movements, with alternating sets of five large-amplitude cycles (20 mm) and five small-amplitude cycles (2 mm). The large-amplitude cycles represent pipe expansion/contraction due to pipeline start-up/shut-down, whereas the small-amplitude cycles correspond to diurnal temperature fluctuations.

3.2 Case Study B: HDPE Pipe in Sand (Weidlich and Achmus 2006, 2008)

The Weidlich and Achmus (2006, 2008) testing chamber measured 0.9 m wide, 1.36 m long and 0.9 m high. The pipe used for the tests was made from HDPE with D = 0.14 m (DN65) and were buried to h/D = 1.5 and 3 in dry quartz sand with D_r = 0.4, 0.5, and 0.7. Key soil properties are presented in Table 1. The tests involved application of ten 50 mm axial displacement cycles using an electrical actuation (push-pull) system.

3.3 Case Study C: HDPE Pipe in Sand (Bilgin et al. 2009)

The Bilgin et al. (2009) testing chamber measured 0.915 m wide, 1.22 m long, and 0.90 m high. An HDPE pipe with *D* = 0.168 m and a wall thickness of 15 mm was used. The pipe was buried to a depth of *H/D* ≈ 4.75 in sand with a relative compaction of about 94%. The soil backfill properties are summarized in Table 1. The test involved ten axial displacement cycles of 25 mm amplitude using a steel reaction frame.

4 Numerical Modelling

4.1 Overview of the Proposed Hybrid-Winkler-Interface (HWI) Approach

The proposed HWI approach is a hybrid formulation consisting of beam elements (representing the pipe structure), Winkler springs orientated in the vertical-uplift, vertical-bearing and lateral directions (representing the soil mass) and a layer of solid 'thin-layer' interface element (representing the soil-pipe interface). The solid thin-layer interface element is based on the bounding surface plasticity constitutive model described in Saberi et al. (2016, 2017, 2018a, 2019a) while the Winkler soil-springs are compatible with the widely used formulations recommended in ALA (2001, 2005).

The circumference of a buried pipe has four salient locations: the crown, two springlines and invert as illustrated in Figure 4. The present model simulates the SPI at these locations using 2-D models in the respective directions, as shown in Figure 5. The Winkler springs at the pipe

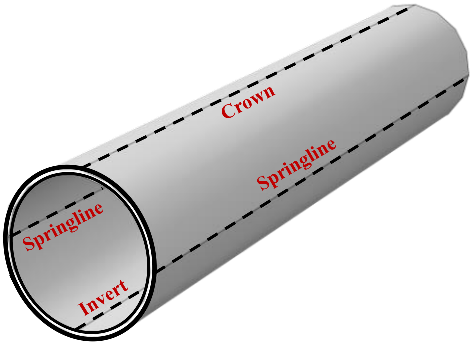

Figure 4. Salient locations around the pipe circumference

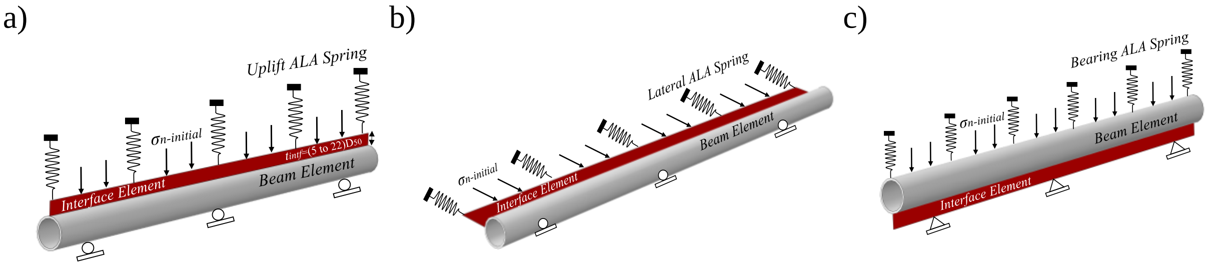

Figure 5. Proposed modeling approach for soil-pipe interaction analysis at the pipe a) crown, b) springlines, and c) invert.

crown (see Figure 5-a) are defined using the bi-linear (elastic-perfectly plastic) behaviour for vertical-uplift force-displacement relationship presented in ALA (2001, 2005) by:

$$Q_u = N_{cv} cD + N_{qv} \gamma' HD \quad \text{3a}$$

$$N_{cv} = 2\left(\frac{H}{D}\right) \leq 10 \quad \text{3b}$$

$$N_{qv} = \left(\frac{\phi H}{44D}\right) \leq N_q \quad \text{3c}$$

$$N_q = exp(\pi \tan \phi) \tan^2(45 + {}^{\phi}/_{2}) \quad \text{3d}$$

$$\begin{aligned} &\Delta_{qu}=0.01H \text{ to } 0.02H \text{ for dense to loose sands} < 0.1D \\ &\Delta_{qu}=0.1H \text{ to } 0.2H \text{ for stiff to soft clays} < 0.2D \end{aligned} \quad \text{3e}$$

where Q_u is the maximum uplift soil resistance per unit length of pipe, c is the soil cohesion, N_{cv} is the undrained vertical-uplift factor and N_{qv} is the drained vertical-uplift factor. Δ_{qu} is the vertical displacement at maximum soil resistance. An initial normal stress ($\sigma_{n\text{-}initial}$) is also applied on the top edge of this interface element to simulate the overburden pressure in the initial state.

Similarly, the springs at the springline position (see Figure 5-b) are defined by:

$$P_u = N_{ch} cD + N_{qh} \gamma' HD \quad \text{4a}$$

$$N_{ch} = a + bx + \frac{c}{(x+1)^2} + \frac{d}{(x+1)^3} \leq 9 \quad \text{4b}$$

$$N_{qh} = a + bx + cx^2 + dx^3 + ex^4 \quad \text{4c}$$

$$\Delta_p = 0.04\left(H + \frac{D}{2}\right) \leq 0.1D \text{ } to \text{ } 0.15D \quad \text{4d}$$

Table 2 Parameters for determination of N_{ch} and N_{qh} (ALA 2001)

Factor	ϕ **(º)**	**x**	**a**	**b**	**c**	**d**	**e**
N_{ch}	0	H/D	6.752	0.065	-11.063	7.119	-
N_{qh}	20	H/D	2.399	0.439	-0.03	1.059×10^{-3}	-1.754×10^{-5}
N_{qh}	25	H/D	3.332	0.839	-0.09	5.606×10^{-3}	-1.319×10^{-4}
N_{qh}	30	H/D	4.565	1.234	-0.089	4.275×10^{-3}	-9.159×10^{-5}
N_{qh}	35	H/D	6.816	2.019	-0.146	7.651×10^{-3}	-1.683×10^{-4}
N_{qh}	40	H/D	10.959	1.783	0.045	-5.425×10^{-3}	-1.153×10^{-4}
N_{qh}	45	H/D	17.658	3.309	0.048	-6.443×10^{-3}	-1.299×10^{-4}

where P_u is the maximum lateral soil resistance per unit length of pipe, N_{ch} and N_{qh} are the undrained and drained lateral bearing capacity factors, respectively, which are determined using Equation 4 and Table 2. Δ_p is the lateral displacement required to mobilise P_u. For the springline model, $\sigma_{n\text{-}initial}$ represents the initial lateral earth pressure at the springline elevation.

Finally, the force-displacement relationship for the soil springs at the pipe invert (see Figure 5-c) is determined using ALA (2001, 2005) as follows:

$$Q_d = N_c cD + N_q \gamma' HD + 0.5 N_\gamma \gamma D^2 \quad \text{5a}$$

$$N_c = [\cot(\phi + 0.001)]\left\{exp[\pi \tan(\phi + 0.001)]\tan^2\left(45 + \frac{(\phi + 0.001)}{2}\right) - 1\right\} \quad \text{5b}$$

$$N_\gamma = exp(0.18\phi - 2.5) \quad \text{5c}$$

$$\Delta_{qd}=0.1D \text{ for granular soils} \quad \text{5d}$$
$$\Delta_{qd}=0.2D \text{ for cohesive soils}$$

where Q_d is the maximum vertical bearing soil resistance per unit length of pipe, γ is the total unit weight of soil, N_c, N_q (evaluated using Eq. 3d), and N_γ are the bearing capacity factors in the vertical-bearing direction, and Δ_{qd} is the downward displacement required to mobilise the maximum bearing resistance. In this instance, the applied $\sigma_{n\text{-}initial}$ represents the overburden pressure. Thus, the initial stress applied on the interface zone is the summation of the overburden pressure and the weight of the pipe including the transported medium. In the modelling process, the axial displacement is applied directly to the beam elements.

The total resultant contact force over the pipe cross section can be obtained from the HWI model by considering the soil spring stiffness as the average values of the three stiffnesses in the vertical-uplift, vertical-bearing and lateral directions (ALA 2001, 2005). The initial normal stress can be calculated using Eq. 1a, which is the average normal stress acting on the pipe.

4.2 Soil-Pipe Interface Modelling

In this study, the coupling between shear and normal deformations is captured using the solid thin-layer interface elements. These elements make use of an advanced 2-D interface constitutive model based on bounding surface plasticity theory and CSSM (Saberi et al. 2017, 2019) . This model was implemented in ABAQUS (Dassault Systèmes 2013) using a user-subroutine ('UMAT') in conjunction with four-node quadrilateral isoparametric thin-layer elements. This model has been shown to capture complex interface behaviour including stress hardening/softening, cyclic stress degradation, dilation and accumulative contraction, stress stabilization, and particle breakage for both monotonic and cyclic shearing (Saberi et al. 2017, 2019). A summary of the constitutive formulations is presented in Table 3.

If the initial normal stress $\sigma_{n\text{-}initial}$ is not available from experimental measurement, $\sigma_{n\text{-}initial}$ can be estimated as the overburden pressure for the crown location and the summation of the overburden pressure and pipe weight for the invert location. For the springline location, the horizontal pressure ($\sigma_{n\text{-}initial}$ in Figure 5-b) can be determined as $K\sigma_v$ where K is the coefficient of lateral earth pressure which varies between ~0.5 and ~1 for loose to dense sands (Wijewickreme et al. 2009). To model the experiments described by Sheil et al. (2018), measured values of $\sigma_{n\text{-}initial}$ were used directly. For the Weidlich and Achmus (2006, 2008) and Bilgin et al. (2009) experiments, $\sigma_{n\text{-}initial}$ is estimated using Eq. 1a.

4.3 Finite Element Model

Figure 5 shows a family of three 'linked' 2-D FE models to simulate the critical locations of the embedded pipe. The models were 1.31 m, 1.2 m and 1.2 m long to simulate the experiments described in Sheil et al. (2018), Weidlich and Achmus (2006, 2008) and Bilgin et al. (2009), respectively. The thickness of the thin-layer interface elements (t_{intf}) can be assumed between 5

Table 3 Constitutive equations of the interface model and model parameters

Constitutive formulation	Eq.	Description	Parameters
Elasticity			
$\dot{\boldsymbol{\sigma}} = \mathbf{D}^{e}\dot{\boldsymbol{\varepsilon}}^{e} = \begin{bmatrix} D_n & 0 \\ 0 & D_t \end{bmatrix}\dot{\boldsymbol{\varepsilon}}^{e} = \begin{bmatrix} D_{n0}\sqrt{\sigma_n/p_{atm}} & 0 \\ 0 & D_{t0}\sqrt{\sigma_n/p_{atm}} \end{bmatrix}\dot{\boldsymbol{\varepsilon}}^{e}$	6	▪ $\boldsymbol{D}^{e}$: elastic stiffness matrix ▪ D_n: elastic normal stiffness ▪ D_t: elastic tangential stiffness ▪ p_{atm}: atmospheric pressure, given by ▪ 101(kPa)	D_{n0} and D_{t0}
Elasto-plasticity			
Yield surface			
$f = (\mu - \alpha) \mp m = \frac{\tau}{\sigma_n} - \alpha - sm = 0$	7	▪ f: yield surface function ▪ τ/σ_n: stress ratio (μ), ▪ α: back-stress-ratio and the slope of yield surface bisector (i.e. $\alpha = \mu - m$) ▪ m: controls the size of the yield surface, given by $0.01\mu^{cs}$-$0.05\mu^{cs}$ ▪ s: auxiliary parameter	
$s = \begin{cases} +1 & \mu - \alpha \geq 0 \\ -1 & \mu - \alpha < 0 \end{cases}$	8		
Critical state			
$\psi = e - e_{cs}$	9	▪ ψ: state parameter ▪ e: void ratio at the current state ▪ e_{cs}: critical state void ratio corresponding to the current value of σ_n. ▪ w_p: modified plastic work ▪ < >: Macaulay brackets; <x>= x if x>0, and <x>= 0 if x≤0. ▪ τ^{cs}: shear stress at critical state ▪ σ_n^{cs}: normal stress at critical state ▪ μ^{cs}: slope of the critical state surface in σ_n-τ plane (i.e. critical state stress ratio)	e_{cs-0}, λ, b_{r1}, b_{r2} and μ^{cs}
$e_{cs} = e_{cs-0}(1 - \frac{w_p}{b_{r1} + b_{r2}w_p}) - \lambda \ln(\sigma_n/p_{atm})$	10		
$W_p = \int \left(\sigma_n \langle \dot{\varepsilon}_n^p \rangle + \tau \dot{\varepsilon}_t^p\right)$	11		
$\tau^{cs}/\sigma_n^{cs} = \mu^{cs}$	12		
Dilatancy			
$\mu^{d} = \mu^{cs}\exp\left(K^{d}\psi\right)$	13	▪ μ^{d}: dilatancy stress ratio ▪ D: dilatancy coefficient ▪ Γ: loading ▪ $\boldsymbol{R}$: direction of increment of plastic strain vector ▪ $\boldsymbol{n}$: vector normal to yield surface f ▪ K_p; plastic modulus ▪ $\mu<\mu^{d}$; contracting response (D>0) ▪ $\mu>\mu^{d}$; dilatant response (D<0) ▪ D=0; zero volumetric rate response ▪ $\boldsymbol{R} \neq \boldsymbol{n}$; non-associated flow rule	K^{d} and A^{d}
$D = \frac{\dot{\varepsilon}_n^p}{\lvert\dot{\varepsilon}_t^p\rvert} = A^{d}\left(d^{d}\right) = A^{d}(\mu^{d} - s\mu)$	14		
$\dot{\boldsymbol{\varepsilon}}^{\mathbf{p}} = \begin{Bmatrix} \dot{\varepsilon}_n^p \\ \dot{\varepsilon}_t^p \end{Bmatrix} = \Gamma\mathbf{R}$	15		
$\Gamma = \mathbf{n}^{\mathbf{T}}\dot{\sigma}/K_p$	16		
$\mathbf{R} = \begin{Bmatrix} R_n \\ R_t \end{Bmatrix} = \begin{Bmatrix} D \\ \partial f/\partial\tau \end{Bmatrix} = \begin{Bmatrix} D \\ s \end{Bmatrix}$	17		
$\mathbf{n} = \begin{Bmatrix} \partial f/\partial\sigma_n \\ \partial f/\partial\tau \end{Bmatrix}$	18		
Plastic modulus			
$K_p = K_{p0}D_{t0}\sqrt{{\sigma_n}/{p_{atm}}}\,\frac{\left(\mu^{f} - s\mu\right)}{\lvert\alpha\rvert}$	19	▪ μ^{f}: failure or peak stress ratio ▪ $K_p > 0$; hardening behaviour ▪ $K_p < 0$; softening behaviour	K_{p0} and K^{f}
$\mu^{f} = \mu^{cs}\exp\left(-K^{f}\psi\right)$	20		
Kinematic hardening			
$\dot{\alpha} = \Gamma\frac{K_p}{s\sigma_n}$	21	▪ $\dot{\alpha}$: back-stress-ratio rate for evaluation of yield surface	
Elasto-plastic stress–strain rate relation			
$\dot{\boldsymbol{\sigma}} = \mathbf{D}^{ep}\dot{\boldsymbol{\varepsilon}} = \left(\mathbf{D}^{e} - \frac{\mathbf{D}^{e}\,R\,n^{T}\,\mathbf{D}^{e}}{K_p + n^{T}\mathbf{D}^{e}R}\right)\dot{\varepsilon}$	22	▪ $\boldsymbol{D}^{ep}$: elasto-plastic stiffness matrix	

and 22 times the mean particle size of the surrounding soil (D_{50}) based on laboratory observations well documented in the literature (Hammad 1991, DeJong and Westgate 2009, Pra-Ai 2013, Martinez et al. 2015, Vangla and Latha Gali 2016, Rui et al. 2021, Vafaei et al. 2021); a thickness of 7 mm was selected here. The boundary conditions are shown in Figure 5. It is worth mentioning that the soil springs are connected to undeformed interface element nodes after the initial normal stress is applied.

5 Model calibration

5.1 Interface model parameters and verification

The HWI interface constitutive model requires eleven parameters: two for elasticity (D_{n0} and D_{to}), three for critical state ($e_{cs\text{-}0}$, λ and μ^{cs}), two for dilatancy (A^d and K^d), one for hardening (k_{p0}), one for failure (k^f), and two for particle breakage (b_{r1} and b_{r2}) (see Table 3). All parameters have a physical meaning and are readily determined using two standard interface shear tests, namely the constant normal load (CNL) and constant normal stiffness (CNS) shear tests. A range of applied normal stresses in those tests is also required. Further information on the model calibration process is available in Saberi et al. (2017, 2019).

5.1.1 Model Calibration for Case Study A (Sheil et al. 2018)

CNL or CNS direct/simple shear testing was not performed as part of the experimental programme described by Sheil et al. (2018, 2021). Consequently, the model was calibrated using measurements obtained directly from test scenario II including (a) local shear and normal contact stress measurements around the pipe circumference and their development during the first axial cycle only and (b) the pipe settlement during the first five axial cycles. The different initial stress regimes at the pipe crown, springline and invert proved convenient for calibrating the input parameters of the interface constitutive model. Data from test scenario II was selected for calibration as an intermediate case though it is expected that calibration against the other test scenarios would have proved equally effective.

Elasticity parameter D_{t0} is calculated using Equation 6 where D_t is determined from the initial slope of the shear stress (τ)-axial displacement (Δ) relationship (shown graphically in Figure 6-a). The elastic normal stiffness D_n is taken to be $1.7D_t$ which has been shown to be a good approximation for granular soil-structure interaction (Ghionna and Mortara 2002, Saberi et al. 2016, 2020a, 2020b). If the shear stresses at critical state (τ_{cr}) (points *a* and *b* in Figure 6-a) are plotted against the corresponding normal stresses ($\sigma_{n\text{-}cr}$) (points a' and b′ in Figure 6-b), the slope of a best fit line between the points (a'' and b'' in Figure 6-c) forced through the origin gives μ^{cs} (see Figure 6-c).

Plotting the critical void ratios (e_{cs}) as a function of the corresponding values of $\ln(\sigma_n/p_{atm})$ allows λ and $e_{cs\text{-}0}$ to be determined as the slope and intercept (respectively) of a best fit line through the points (see Figure 6-d). The void ratio increment at the interface can be calculated as $de = (1 + e_{in})(du_n/t_{intf})$, where e_{in} is the initial void ratio, and du_n is the normal displacement increment at the interface zone.

The positive parameter K^f controls the post-peak softening response and is defined as:

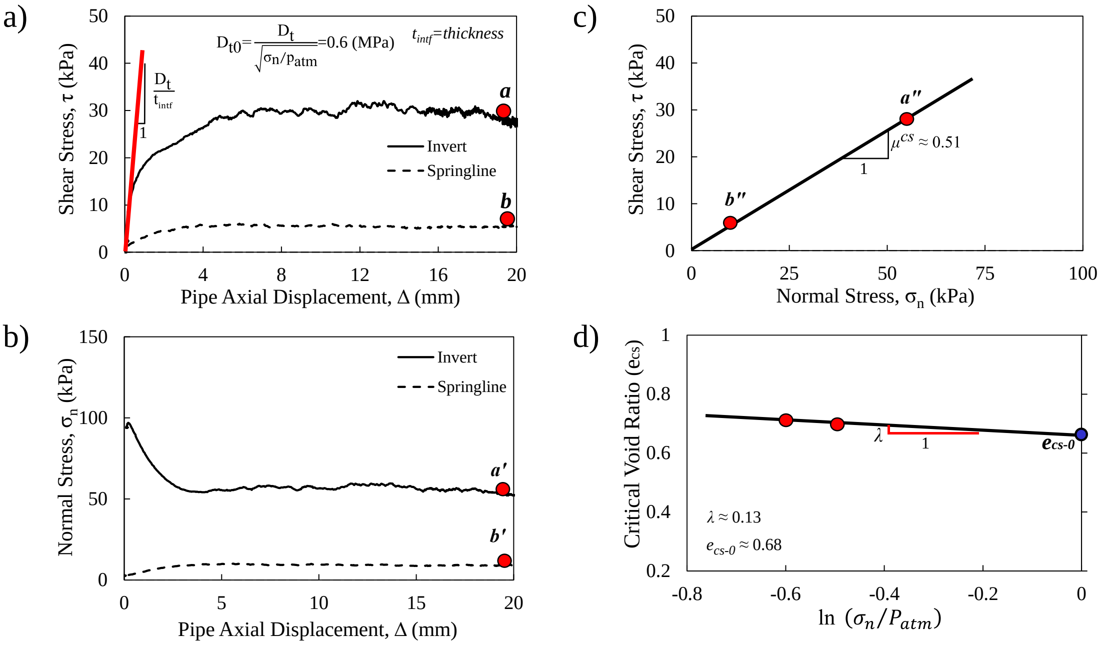

Figure 6. Illustration of the calibration process for interface model parameters of D_{t0}, μ^{cs}, $e_{cs\text{-}0}$, and λ for Hostun sand (Sheil et al. 2018). See Table 3 for description of parameters.

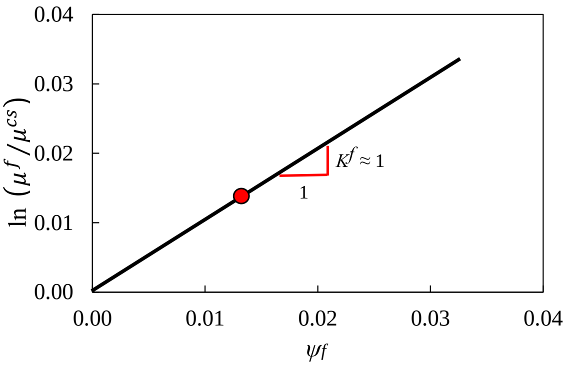

Figure 7. Representation for calibration of the interface model parameter k^f for Hostun sand by Sheil et al. (2018).

$$K^f = \frac{ln(\mu^f/\mu^{cs})}{\psi_f} \tag{23}$$

where μ^f is the peak stress ratio and ψ_f is the state parameter at peak. Parameter K^f can be determined as the slope of a best fit line passing through the origin in ψ_f - ln (μ^f/μ^{cs}) space as shown in Figure 7. In this case, only a single data point was available to calibrate K^f. Parameters μ^f and ψ_f can be determined using peak values in the τ-u_t and u_n-u_t planes.

Parameters K^d and A^d were determined by matching the model predictions and laboratory test data for normal stress (σ_n)-pipe axial displacement (Δ) relationships. Only the data related to the first axial displacement cycle of test scenario II was used for this purpose. Figure 8 presents the results of this calibration exercise using $K^d = 2$ and $A^d = 0.8$. Figure 9 shows the sensitivity of the development of σ_n to A^d and k^d.

If data at the phase transformation state are available, the parameter K^d is calculated similar to K^f using Equation 24.

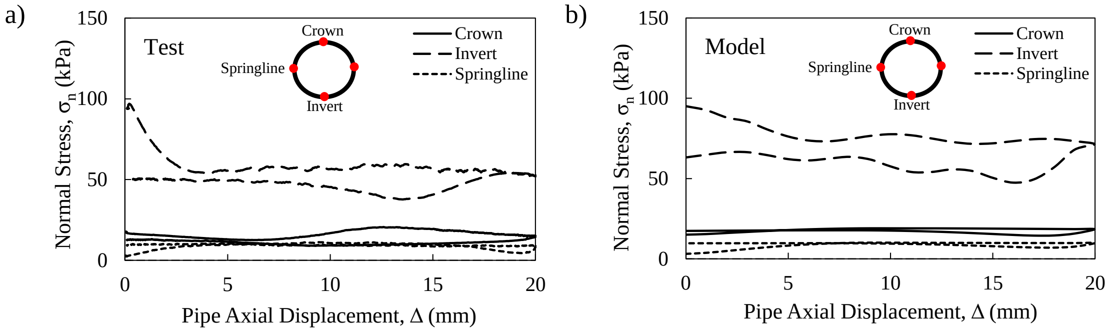

Figure 8. Calibration of model predictions using experimental measurements of local normal contact stresses for Hostun sand for test scenario II (Sheil et al. (2018)); a) measured σ_n-Δ, and b) predicted σ_n-Δ.

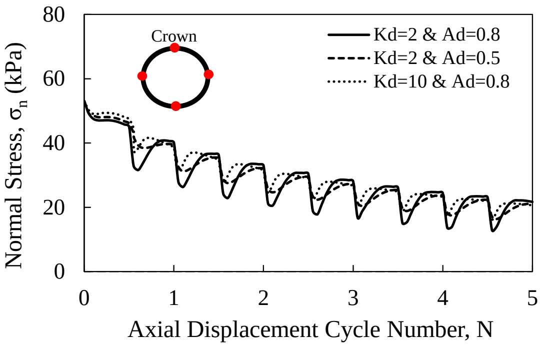

Figure 9. Sensitivity analysis on the interface constitutive model parameters K^d and A^d

$$K^d = \frac{ln(\mu^{phts}/\mu^{cs})}{\psi_{phts}} \tag{24}$$

Where μ^{phts} and ψ_{phts} are stress ratio and state parameters in phase transformation. The parameter A^d can be also determined using the measured u_n-Δ relationship in soil-pipe tests and/or u_n-u_t from CNL/CNS tests, where u_n and u_t are the normal and tangential displacements respectively. For a large-deformation problem, Equation 14 can be recast as follows:

$$A^d \approx \frac{(du_n/|du_t|)}{\mu^d - \mu} \tag{25}$$

where du_n and du_t are incremental displacements; an average value of A^d is recommended for use in the interface model.

Parameter K_{p0} was calibrated by fitting model predictions to the measured development of local τ with Δ from test scenario II, as shown in Figure 10 (calibrated $K_{p0} = 0.075$). Alternatively, one can simply derive the following relationship for an interface shear test under CNL condition:

$$\frac{du_t}{t_{intf}} = \left(\frac{1}{D_t} + \frac{1}{K_p}\right) d\tau \tag{26}$$

where $d\tau$ is the shear stress increment. By substituting Equation 19 into Equation 26, K_{p0} can be evaluated as:

$$K_{p0} = \frac{|\alpha|}{(\mu^{cs} - \mu)\left(\left(D_t \frac{du_t}{t_{intf} d\tau}\right) - 1\right)} \tag{27}$$

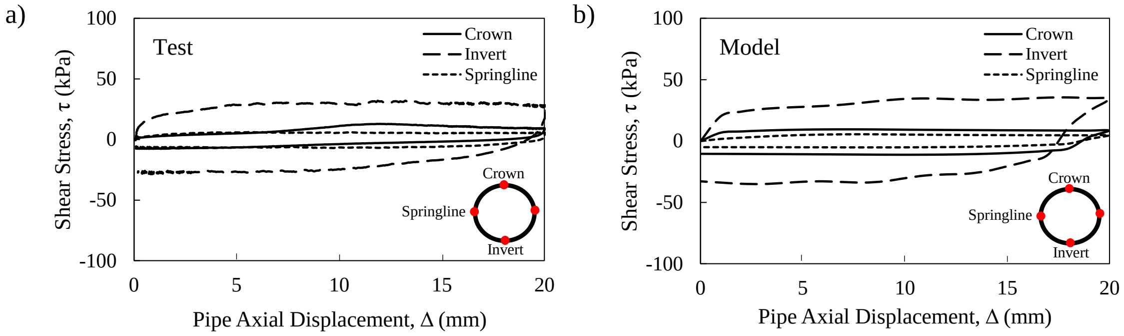

Figure 10. Calibration of model predictions using experimental measurements of local shear contact stresses for Hostun sand for test scenario II (Sheil et al. 2018); a) measured τ-Δ, and b) predicted τ-Δ.

The parameters b_{r1} and b_{r2} control cyclic volumetric contraction behaviour at the interface and can be determined from the particle breakage index (B_r) and total plastic work using existing methods such as that described in Lade et al. (1996). More information regarding the plastic work and boundary condition effects on the sand particle breakage under shearing can be found in Vafaei et al. (2019). In this study, b_{r1} and b_{r2} were determined by fitting model predictions to the measured development of pipe settlement in the first five cycles. Figure 11 presents a brief sensitivity study including the results using the final fitted parameters (b_{r1}=0.3 MP and b_{r2}=0.4). The deviation between test results and model predictions in the first two cycles, can be explained by the soil spring stiffness values computed by ALA (2001, 2005). A summary of the calibrated model parameters is provided in Table 4 including the authors' suggested ranges.

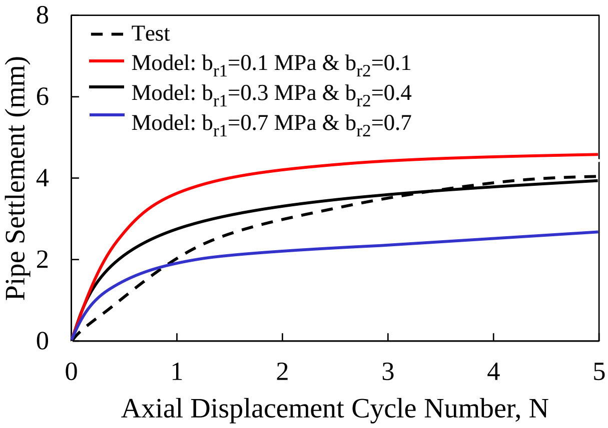

Figure 11. Representation for calibration of particle breakage parameters b_{r1} and b_{r2} of the interface model for Hostun sand (Sheil et al. 2018).

Table 4 Calibrated parameters for the interface constitutive model

Parameters	Hostun sand (Sheil et al. 2018)	Quartz sand (Weidlich and Achmus 2006, 2008)	Sand (Bilgin et al. 2009)	Authors' suggested range
D_{t0} (*MPa*)	0.6	0.4	0.4	0.2-15
D_{n0} (*MPa*)	1	0.5	0.5	0.2-15
$e_{cs\text{-}0}$	0.68	0.62	0.54	0.25-1.2
λ	0.13	0.01	0.01	0.01–0.4
μ^{cs}	0.51	0.8	0.56	0.1-0.9
A^d	0.8	0.6	0.6	0.25-1
K^d	2	4	6	0.3-20
K^f	1	5	0	0-7
K_{p0}	0.075	0.4	0.4	0.05-1
b_{r1} (*MPa*)	0.3	4.5	1	0.1-20
b_{r2}	0.4	2	1	0.1-5

Additional practical information that could be useful for design engineers to determine some model parameters are presented in Section 9.

5.1.2 Model Calibration for Case Study B (Weidlich and Achmus 2006, 2008)

As no local contact stress measurements are available, the HWI model was calibrated using measurements of the virgin axial load-displacement response (*h/D* = 1.5 and $D_r = 0.7$) and the development of pipe settlement for the first ten cycles (*h/D* = 1.5 and $D_r = 0.4$). The fitted model parameters are presented in Table 4. As shown in Figure 12, there is very good agreement between model predictions and the laboratory measurements.

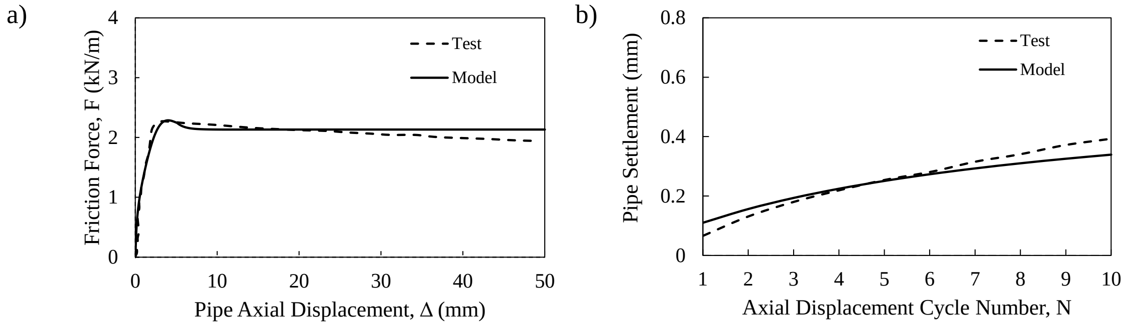

Figure 12. Calibration of model predictions using experimental measurements for quartz sand-HDPE pipe system (Weidlich and Achmus 2006, 2008); a) F-Δ with h/D = 1.5 and D_r=0.7, and b) pipe settlement-N with h/D = 3 and D_r=0.4.

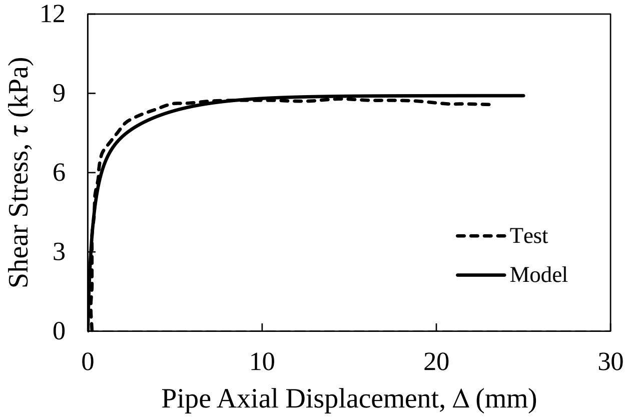

Figure 13. Comparison between model predictions and experimental measurements for sand-HDPE pipe system by Bilgin et al.(2009) used for model calibration.

5.1.3 Model Calibration for Case Study C (Bilgin et al. 2009)

The calibration procedure for Case Study C was similar to that adopted for Case Study B. The HWI model was calibrated using the measures τ-Δ relationship (see Figure 13). As no peak in the stress-displacement response was evident, K^f=0 was selected. Typical values of b_{r1}=1 MPa and b_{r2}=1 were also selected due to the lack of measurement of interface volumetric behaviour or pipe settlement. The calibrated model parameters are presented in Table 4. As shown in

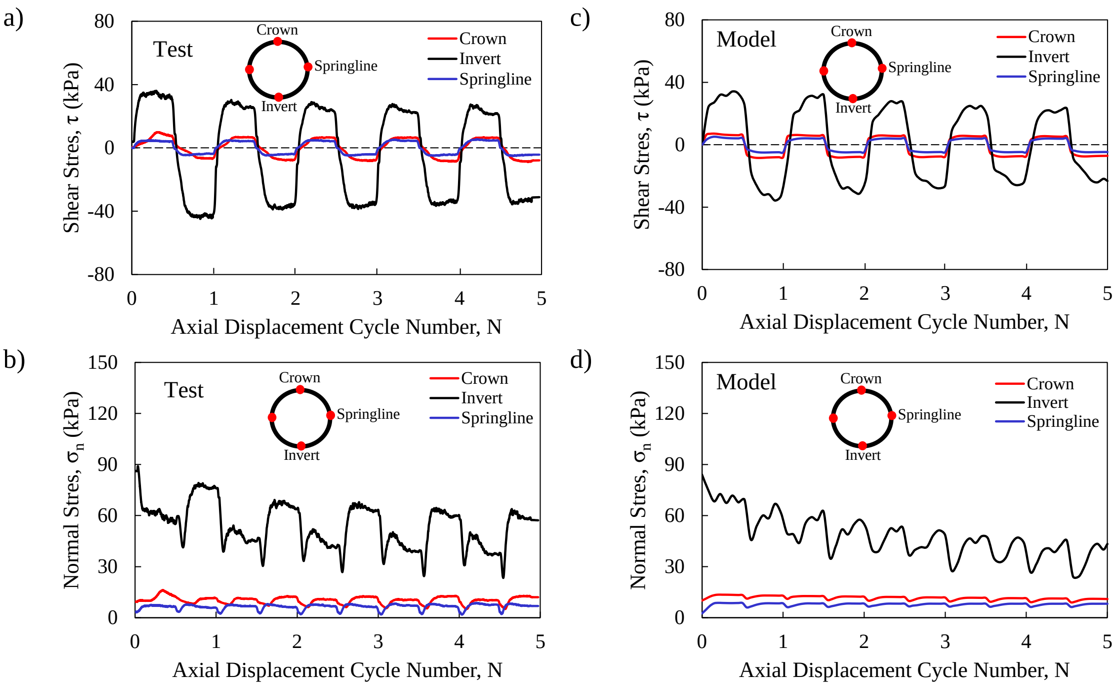

Figure 14. Comparison between model predictions and experimental measurements of contact stress development during cyclic loading for test scenario I, a) measured τ-N, b) measured σ_n-N, c) predicted τ-N, and d) predicted σ_n-N.

Table 5 Input parameters for soil spring force-displacement relationships

	Parameters				
	Cohesion, c′ (kPa)	**Pipe Outside Diameter, D (mm)**	**Effective Unit Weight, γ (kN/m^3)**	**Friction Angle, ϕ' (deg)**	**Depth to pipe centreline, H (m)**
Sheil et al. (2018)	0	350	13.4	37.9	0.675 for test scenario I 1.175 for test scenario II 1.275 for test scenario III
Weidlich and Achmus (2006, 2008)	0	140	15.7 for D_r=0.4 16 for D_r=0.5 16.7 for D_r=0.7	~32 for D_r=0.4 38 for D_r=0.5 ~40 for D_r=0.7	0.28 and 0.49
Bilgin et al. (2009)	0	168	17	~38	0.76

Figure 13, there is excellent agreement between the model simulation and laboratory observations (maximum difference <3%).

5.2 Soil spring and pipe parameters

The input parameters for the soil mass springs (Eqs. 3 - 5) are presented in Table 5 for Case Studies A, B and C. For Case Studies B and C, ϕ' was estimated using the approaches proposed by Mujtaba et al. (2018) and Bowles (1996) respectively. The pipe was modelled as an elastic body with Young's modulus, E = 210 GPa, and Poisson's ratio, v = 0.3 for Case Study A, and E = 0.9 GPa and v = 0.35 for Case Studies B and C.

6 Numerical predictions of Case Study A: Steel Pipe in Hostun Sand

6.1 Test Scenario I

Figure 14 presents comparisons between the experimental measurements (Figure 14-a and 14-b) and numerical predictions (Figure 14-c and 14-d) of the development of shear and normal contact stresses during cyclic loading for test scenario I; results for the crown, invert and springline locations for the first five 20 mm displacement cycles have been considered. The shear stress at the invert location is much higher than at the crown and springline due to the significant pipe weight which is captured in both the measurements and model predictions (see

Figure 14-a and Figure 14-b respectively). The shear stress degrades as cycling progresses, stabilizing after three cycles. This is due to accumulative contraction which results in normal stress degradation and is most noticeable at the invert location. The normal stresses also exhibit transient drops in magnitude immediately following a reversal in the loading direction due to a contraction of the soil-pipe interface. As shown in Figure 14-c and 14-d, the numerical model appears to provide a high-fidelity representation of the measured shear and normal contact stresses (respectively) during cyclic axial loading.

The measurements and numerical predictions are re-plotted in the τ-σ_n plane in Figure 15-a and Figure 15-b respectively. These results highlight the complex local stress paths at the soil-pipe interface and their variation during cycling. From Figure 15-a, the stress paths at all three pipe locations are well-bounded by the estimated Coulomb friction envelope of $\mu^{fric} = 0.53$. The numerical predictions again provide very good agreement with the laboratory measurements and the back-calculated friction envelope (see Figure 15-b).

6.2 Test Scenario II

Shear and normal contact stress measurements for test scenario II are presented in Figure 16-a and 16-b respectively. Degradation of shear stresses at the crown, springline and invert locations again occurs primarily over the first three cycles (Figure 16-a). The normal stresses exerted by the soil on the pipe also degrade with an increase in the number of axial displacement cycle (see Figure 16-b). However, the rate of normal stress degradation in scenario II is more

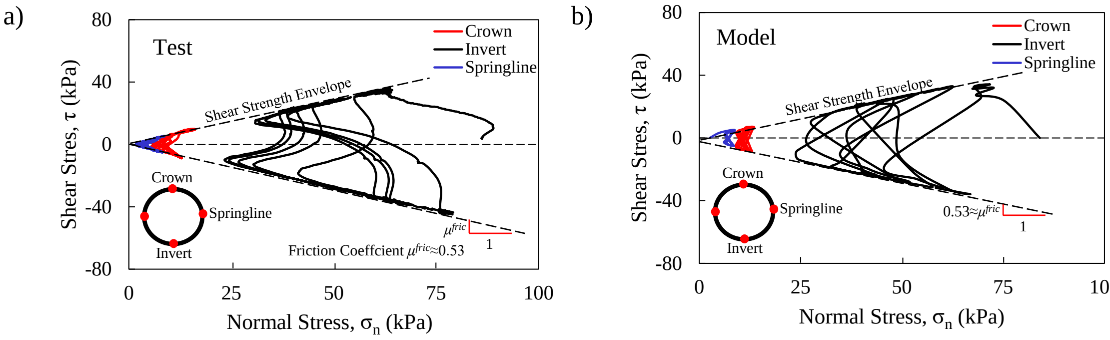

Figure 15. Local contact stress paths at the crown, invert and springline locations for test scenario I, a) laboratory measurements, and b) numerical predictions.

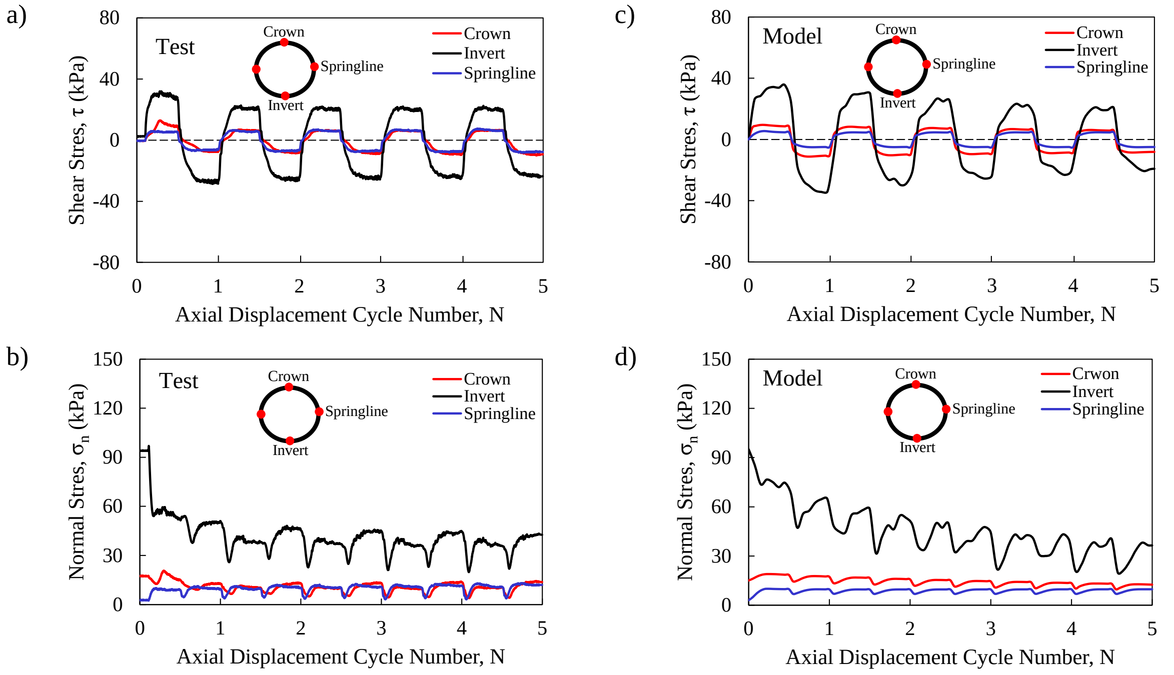

Figure 16. Comparison between model predictions and experimental measurements of contact stress development during cyclic loading for test scenario II, a) measured τ-N, b) measured σ_n-N, c) predicted τ-N, and d) predicted σ_n-N.

significant compared with scenario I; this is due to the increased soil overburden. The greater confinement pressures lead to a greater tendency of the interface to contract during cyclic loading and therefore a greater rate of degradation in normal stress.

While these measurements for the first axial displacement cycle were used for calibration, the HWI model provides accurate predictions of the shear and normal stress responses at the crown, springline and invert locations for the remaining cycles (Figure 16-c and 16-d). The numerical model also predicts the degradation in both τ and σ_n during the test and captures the transient drops in normal stress following a reversal in loading direction (see Figure 16-d).

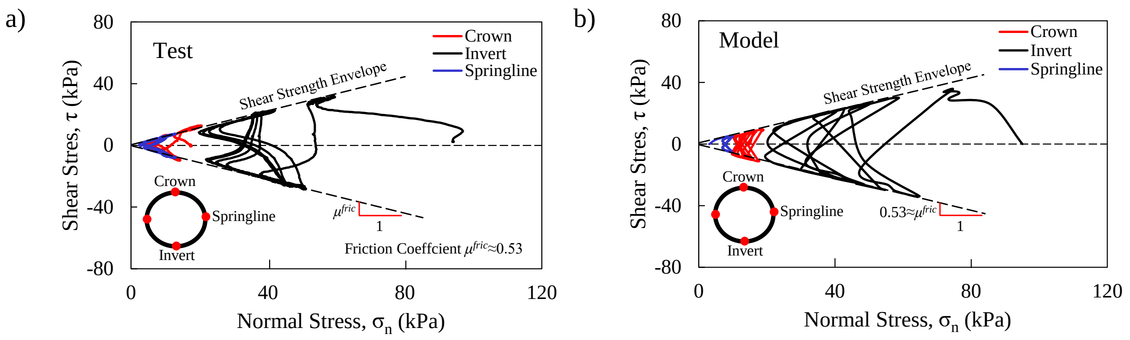

Figure 17. Local contact stress paths at the crown, invert and springline locations for test scenario II, a) laboratory measurements, and b) numerical predictions.

The local stress paths measured at the crown, springline and invert locations are plotted in Figure 17-a. Both τ and σ_n at the soil-pipe interface degrade during cyclic loading which is again more pronounced at the invert location. The friction coefficient envelope of $\mu^{fric} = 0.53$ is again captured by the numerical predictions (see Figure 17-b).

6.3 Test Scenario III

Notably larger contact shear stresses were measured at all three pipe locations during the first cycle for test scenario III compared with scenarios I and II (Figure 18-a). The initial normal stress and the rate of degradation, particularly in the first cycle, at the crown and invert are also significantly greater (Figure 18-b). This is due to a higher volumetric compaction in the initial cycle compared with subsequent cycles. Figure 18-c and 18-d show that there is good agreement between the experimental results and numerical predictions for both shear stress and normal stress development during cycling. Although the general trend for σ_n degradation with increasing N predicted by the HWI model is similar to the measured response, the decrease and subsequent increase in σ_n following load reversals are notably different. This is due to direction-

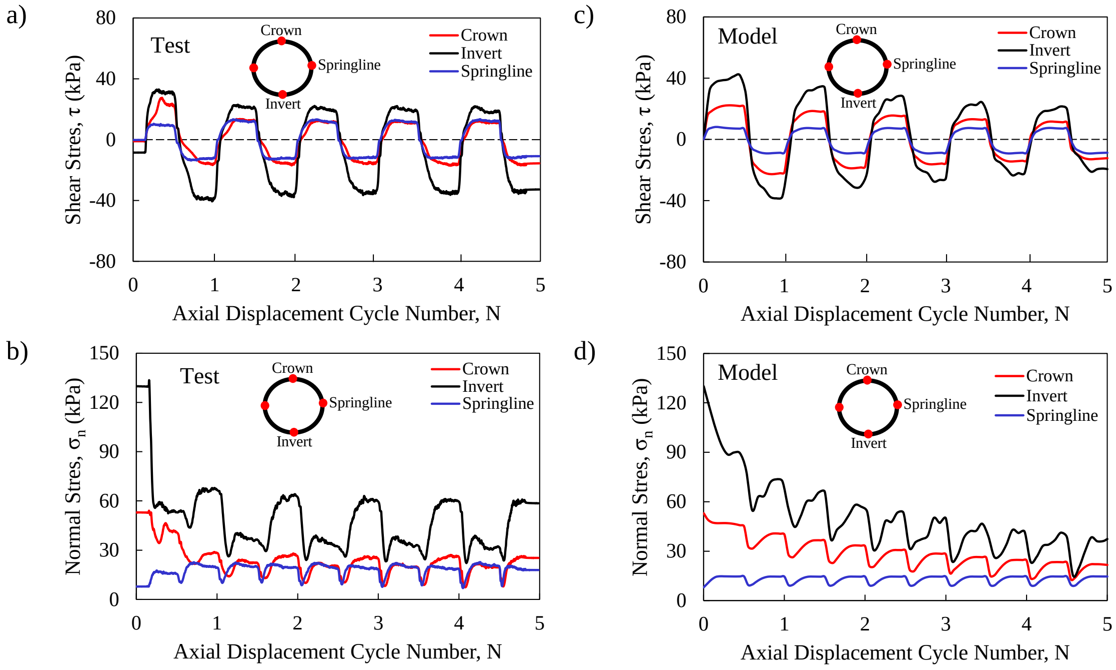

Figure 18. Comparison between model predictions and experimental measurements of contact stress development during cyclic loading for test scenario III, a) measured τ-N, b) measured σ_n-N, c) predicted τ-N, and d) predicted σ_n-N.

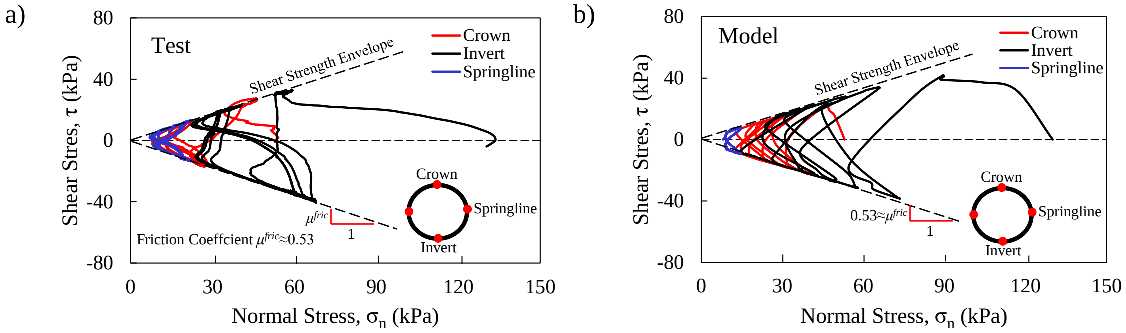

Figure 19. Local contact stress paths at the crown, invert and springline locations for test scenario III, a) laboratory measurements, and b) numerical predictions.

dependent 'aeolotropy of interfaces' which is a common phenomenon in granular soil-structure interface problems (Zhang and Zhang 2009, Martinez et al. 2019, O'Hara and Martinez 2020). It is worth remarking that this phenomenon is yet to be captured within a constitutive model.

The stress degradation in the initial cycles is also observed in the measured stress paths presented in Figure 19-a. The numerical model provides a good representation of the stress paths at all locations including significant degradations in the first cycle especially at the pipe crown and pipe invert locations (Figure 19-b).

6.4 Pipe Settlement

Measurements of pipe settlement during cyclic axial loading for all three test scenarios are presented in Figure 20-a; in this case, only the maximum settlement recorded for a given axial displacement cycle is plotted. As can be observed from Figure 20-a, a large proportion of the total settlement occurs during the first cycle, likely due to significant volumetric contraction within the soil-pipe interface. This phenomenon has been observed for other granular soil-structure interfaces where the interface experiences a larger proportion of compaction in the first shearing cycle compared with subsequent cycles (Fakharian 1996, Shahrour and Rezaie 1997, Saberi et al. 2018b). Corresponding HWI predictions of pipe settlement are shown in Figure 20-b. The model accurately predicts the large proportion of total settlement in the first cycle. The HWI model also correctly simulates the effect of soil cover height on the pipe

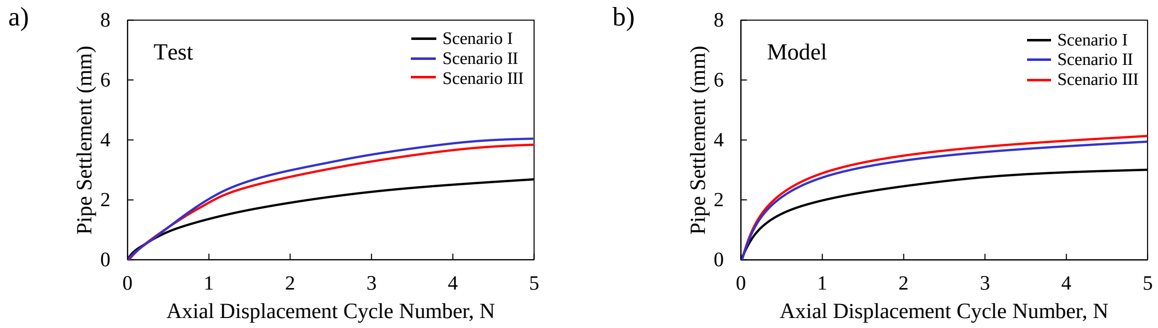

Figure 20. Experimental and numerical modeling comparisons for pipe settlement for all three test scenarios, a) laboratory measurements, and b) numerical predictions.

settlement, indicating that the model provides an accurate description of the stress-dependency of soil behaviour.

6.5 Maximum Contact Stresses

By way of example, HWI predictions of the maximum normal (σ_{n-max}) and shear (τ_{max}) contact stresses for a given cycle number are compared with all three sets of laboratory measurements in Figure 21, Figure 22 and Figure 23 for crown, invert and springline locations respectively. From Figure 21, there is very good agreement between the predictions and measurements at the pipe crown for the three test scenarios. In test scenarios I (Figure 21-a) and II (Figure 21-b), σ_{n-max} experiences a significant dilation-induced increase in magnitude after the first cycle before reducing in the second cycle and subsequently stabilizing at ~12.5 kPa and ~14 kPa, respectively. The HWI model accurately captures these trends with a maximum difference of ~12% for the peak value in the first cycle. However, in test scenario III, the initial normal stress is relatively large such that the soil-pipe interface experiences only contraction during the first five cycles resulting in a 52% degradation in σ_{n-max} (see Figure 21-c). By comparison, the HWI model predicts ~57% degradation.

Similar findings can be deduced from an examination of τ_{max} in Figure 21-d to Figure 21-f for test scenarios I to III respectively. The HWI model accurately simulates the degradation in τ_{max} for the all three test scenarios. For example, τ_{max} degrades after five cycles in test scenario

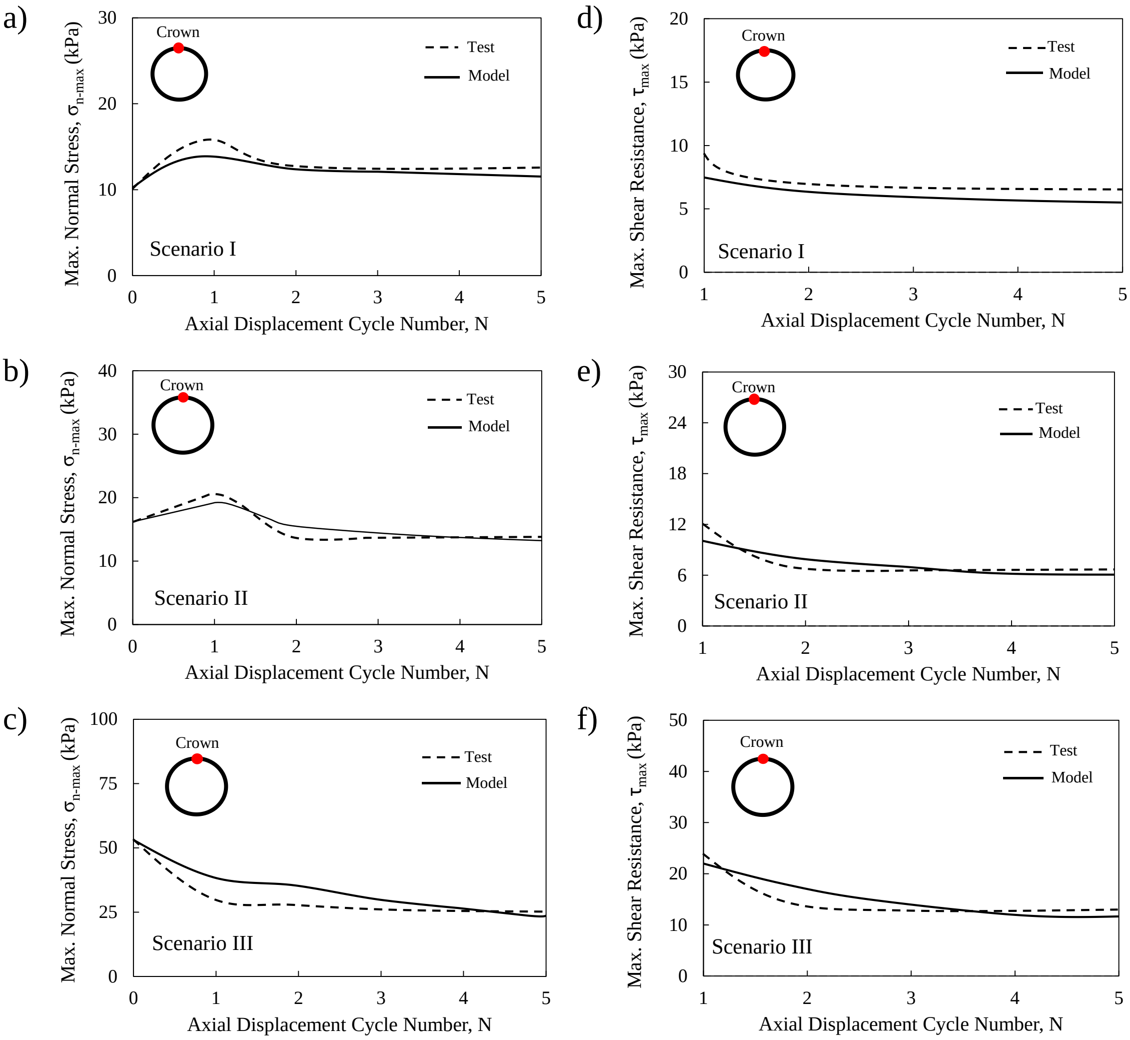

Figure 21. Maximum contact stress variation during cyclic loading at pipe crown; a) $\sigma_{n\text{-}max}$, scenario I, test, b) $\sigma_{n\text{-}max}$, scenario II, c) $\sigma_{n\text{-}max}$, scenario III, d) τ_{max}, scenario I, e) τ_{max}, scenario II, and f) τ_{max}, scenario III.

I (Figure 21-d) ~28% and in scenario III (Figure 21-f) ~50%. The HWI model predicts these degradations with ~2% and ~4% differences respectively.

Owing to the larger normal stress, the soil-pipe interface contracts at the invert location for all three test scenarios which stabilizes after approximately three cycles (Figure 22). This behaviour leads to a significant degradation in both $\sigma_{n\text{-}max}$ (see Figure 22-a to c) and τ_{max} (see Figure 22-d to f) during the first three cycles before stabilizing. The HWI model reproduces this behaviour in all three test scenarios. The maximum degradations occur in test scenario III in which $\sigma_{n\text{-}max}$ (Figure 22-c) and τ_{max} (Figure 22-f) degrade ~55% and ~40% respectively during the five cycles. These considerable degradations have been simulated by the HWI model: ~63%

for $\sigma_{n\text{-}max}$ and ~48% for τ_{max}. According to Figure 22, the maximum difference between the laboratory data and the model predictions is <16%.

There is again very good agreement between the HWI model predictions and measurements at the pipe springline location during the three test scenarios, as shown in Figure 23. For test scenarios I - III, $\sigma_{n\text{-}max}$ experiences an increase in magnitude over the first cycle which is likely due to dilation at the low initial normal stress at the springline, as shown in Figure 23-a to c. $\sigma_{n\text{-}max}$ stabilizes at ~8.5 kPa, ~12 kPa and ~22 kPa for the test scenarios I, II and III respectively after the second cycle. The HWI simulations deviate from measurements by a maximum of ~9%, ~10% and ~18% in test scenario I, II and III respectively. At the springline, τ_{max}

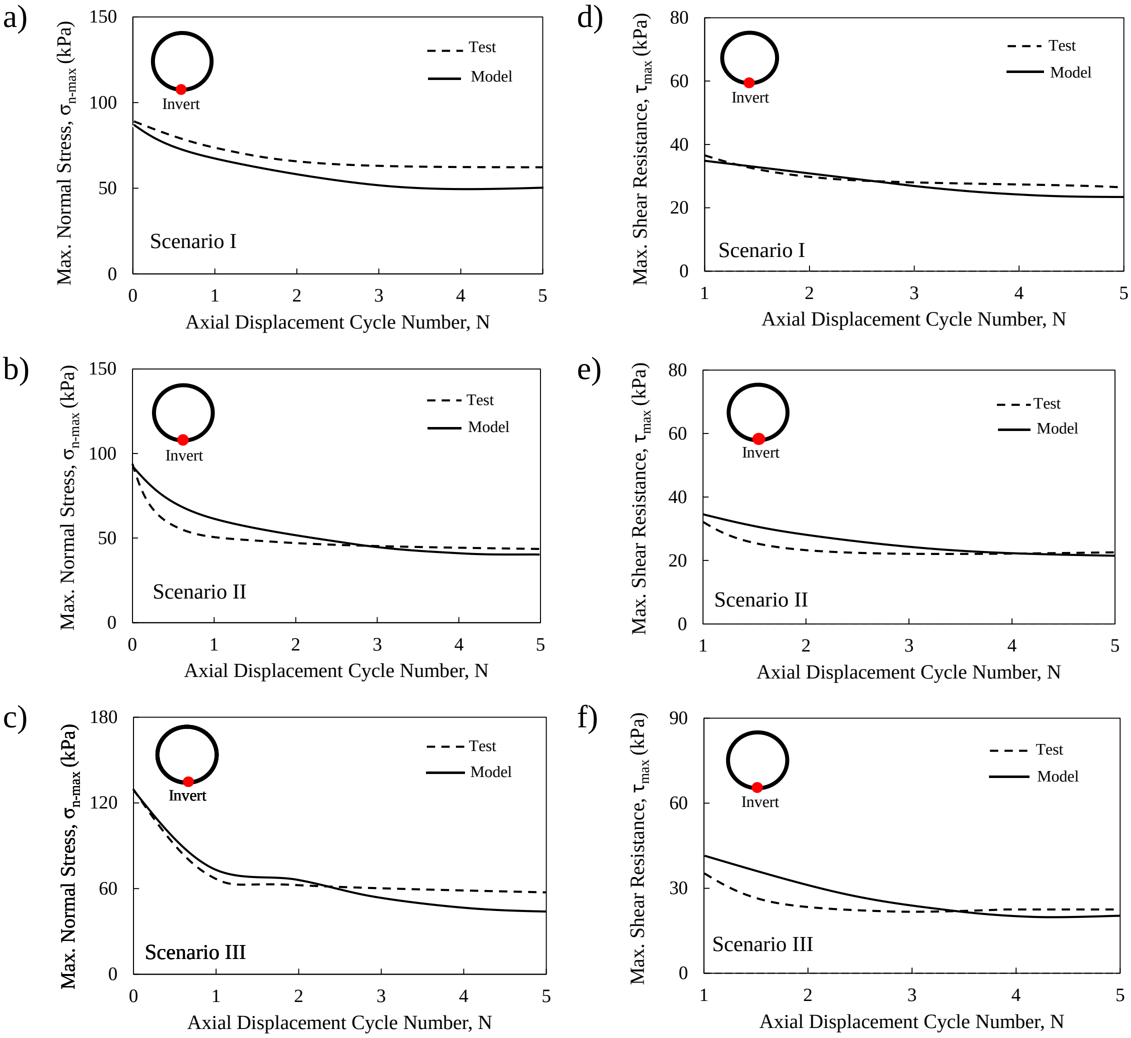

Figure 22. Maximum contact stress variation during cyclic loading at pipe invert; a) $\sigma_{n\text{-}max}$, scenario I, test, b) $\sigma_{n\text{-}max}$, scenario II, c) $\sigma_{n\text{-}max}$, scenario III, d) τ_{max}, scenario I, e) τ_{max}, scenario II, and f) τ_{max}, scenario III.

experiences no significant variation during cycling as the maximum normal stress is low and do not change significantly after the first cycle (Figure 23-d to f). This is also accurately captured by the HWI model.

Due to the large axial displacement amplitude (20 mm), the soil-pipe interface reaches critical state conditions within a given loading cycle. According to the laboratory measurements (Figure 21 to Figure 23), $\sigma_{n\text{-}max}$ and τ_{max} experience another steady state condition after approximately three cycles when both $\sigma_{n\text{-}max}$ and τ_{max} stabilize due to stabilization of accumulative contraction. From Figure 21 to Figure 23, the HWI model captures the steady

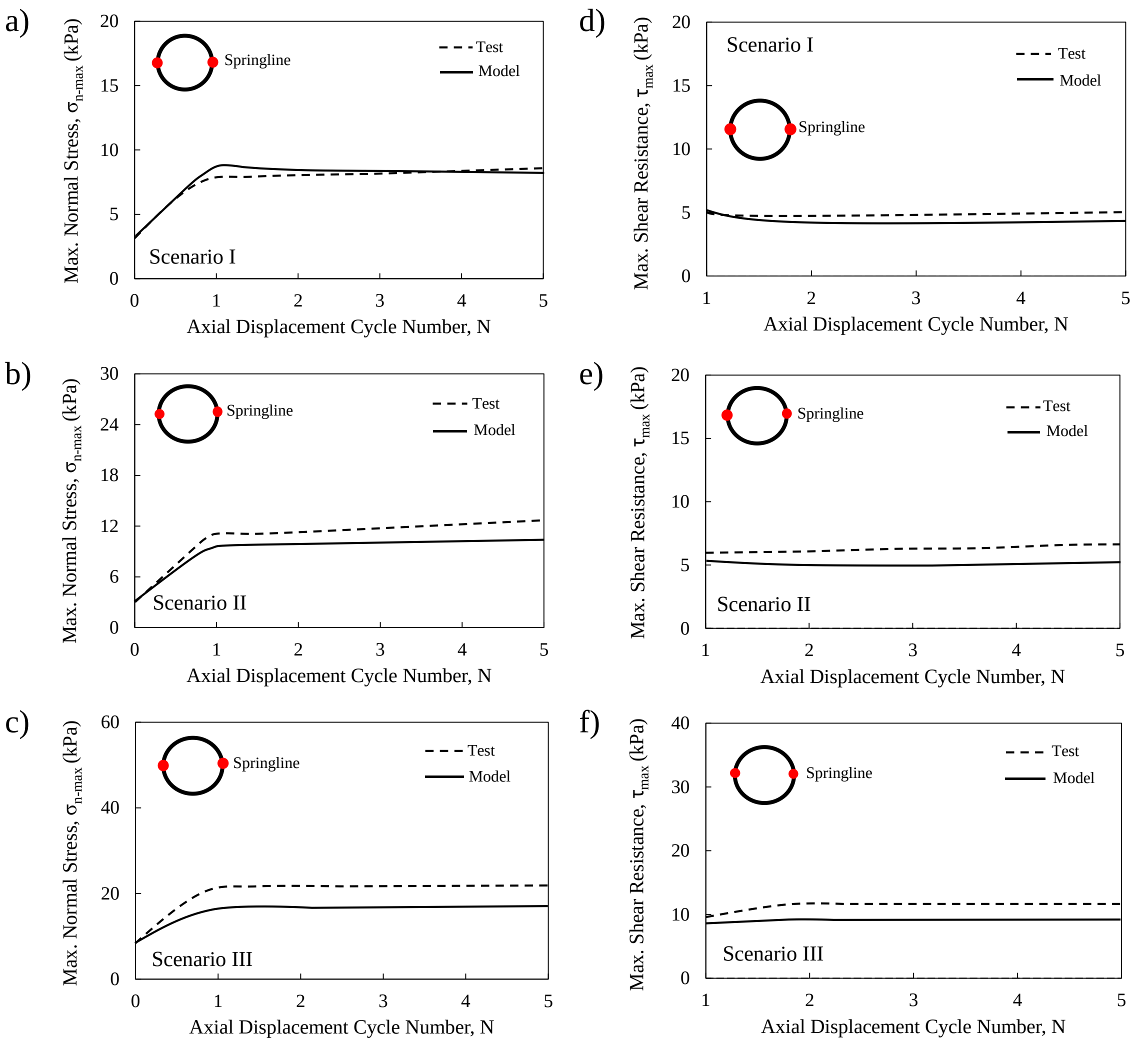

Figure 23. Maximum contact stress variation during cyclic loading at pipe springline; a) $\sigma_{n\text{-}max}$, scenario I, test, b) $\sigma_{n\text{-}max}$, scenario II, c) $\sigma_{n\text{-}max}$, scenario III, d) τ_{max}, scenario I, e) τ_{max}, scenario II, and f) τ_{max}, scenario III.

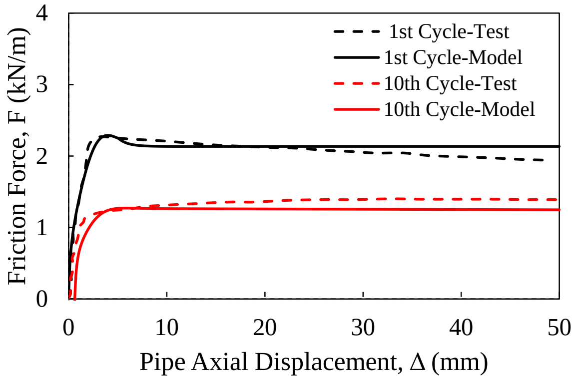

Figure 24. Comparison between model predictions and experimental measurements for quartz sand-HDPE pipe system (Weidlich and Achmus 2006, 2008); F-Δ with h/D=1.5 and D_r =0.7.

state conditions (a) within a given cycle and (b) cumulatively after several cycles when stabilization is reached.

7 Numerical Predictions of Case Study B: HDPE Pipe in Quartz Sand

Present predictions of the pipe load-displacement response for D_r = 0.7 and h/D = 1.5 are compared with laboratory measurements reported by Weidlich and Achmus (2006, 2008) in Figure 24; for clarity, only the first and last cycle are presented. As the soil backfill is dense, the load-displacement response exhibits strain softening behaviour for the first cycle. The friction force experiences significant cyclic degradation (~30%) after ten cycles where a steady state value of ~1.4 kN/m is reached. Similar behaviour has been discussed by Low et al. (2017) for subsea pipelines located on over-consolidated clay. The proposed HWI model captures the measured response very well, including the strain softening, cyclic degradation and steady state friction after ten cycles (maximum deviation in prediction of ~7%).

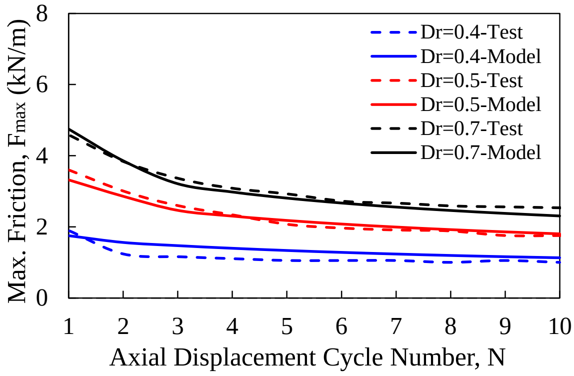

Fi r quartz
sa D_r =0.4,
0.5

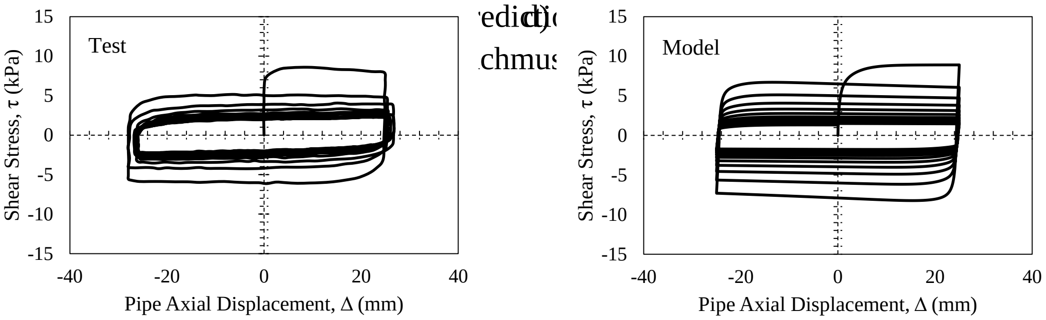

Figure 26. Comparison between model predictions and experimental measurements for sand-HDPE pipe system (Bilgin et al. 2009) in τ-Δ plane; a) test, and b) model.

The influence of D_r on the maximum frictional resistance (F_{max}) developed over a given cycle is presented in Figure 25. In all cases, F_{max} reduces with N where the rate of degradation gradually reduces as cycling progresses, eventually reach steady state after $N \approx 4$. It can be seen that the HWI model captures these responses very well particularly the rate of cyclic degradation in F_{max} with less than 4% deviation compared with measurements. Figure 25 also shows that a decrease in D_r results in a significant reduction in F_{max}. For example, by reducing D_r from 0.7 to 0.4, the steady state F_{max} reduces ~60% in laboratory measurements and ~55% in HWI model predictions.

8 Numerical Predictions of Case Study C: HDPE Pipe in Sand

HWI predictions of the development of shear stress during cyclic loading of a compacted sand-HDPE pipe interface is compared with laboratory observations reported by Bilgin et al. (2009) in Figure 26. The measured τ degrades significantly (~75%) over the course of ten cycles, and this trend is captured by the HWI model very well with a maximum deviation of ~5%. Similar finding can be observed for the τ_{max} developed in each cycle as shown in Figure 27. The rate of degradation also reduces after N ≈ 5 where the τ_{max} tends to reach a steady state condition. This phenomenon is also accurately predicted by the HWI model.

9 Implications for Design

The most popular approach for the determination of the axial resistance of buried pipelines in granular soils is described by Eq. 1. This approach does not capture the complex shear and

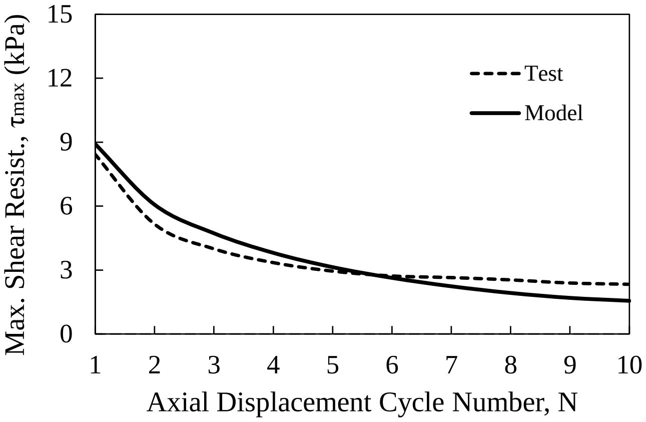

Figure 27. Comparison between model predictions and laboratory testing for τ_{max} against N for buried HDPE pipe (Bilgin et al. 2009).

normal stress distributions and their development during cycling presented in this paper. For practical applications, the proposed model can be calibrated using conventional CNL or CNS direct/simple interface shear tests, in the absence of site specific field or laboratory measurements. Only two direct interface shear tests are necessary with two different applied normal stresses. The interface model parameters can be determined using the methodology described in Saberi et al. (2017, 2019). The key model parameters for prediction are the dilative parameters k^d and A^d and particle breakage parameters b_{r1} and b_{r2}. Parameters A^d and k^d control the amplitude of the normal contact stress oscillation upon reversals in loading direction whereas parameters b_{r1} and b_{r2} control the magnitude of volume contraction and pipe settlement. The interface model can then be employed directly for design in conjunction with the family of soil mass springs described in ALA (2001, 2005).

The pipe surface roughness has a significant influence on the pull-out resistance, normal and shear stress distribution and their variation during axial cyclic loading and should be taken into account in buried pipeline design. Differences in the interface roughness are accounted for through the model parameters A^d, k^d and μ^{cs}.

Based on the experience of the authors, a suggested range for the interface model parameters is suggested in Table 4. This range can be used in the absence of problem-specific information or can serve for the preliminary estimation of soil-pipe interface behaviour under monotonic and cyclic loading. It is worth remarking that only a single set of calibration parameters is required to capture both monotonic and cyclic response, changes in stress level (soil overburden) and soil relative density.

10 Conclusions

In this study, the development of a practical and efficient ‘Hybrid-Winkler-Interface’ (HWI) modelling approach has been described to simulate SPI during cyclic axial loading. Measurements obtained from three full-scale laboratory testing programmes were used to validate the proposed model and evaluate its ability to predict complex SPI behaviour. These experimental data cover different burial depths, soil relative densities and different pipe materials. The measurements included distributions of both shear and normal stresses around the pipe, maximum shear resistance and their variations with the number of axial displacement cycles as well as pipe settlement. The key conclusions from this study are as follows:

- The integrated response of the soil-pipe interaction problem including stress distributions around the pipe and their variations under cyclic loading can almost entirely be described by detailed soil-structure interface mechanics.
- The invert of the buried pipe experiences the maximum initial shear and normal stresses induced by the soil. Both shear and normal stresses acting on the crown, springline and invert of the buried pipe degrade during cyclic loading and stabilize after 2-3 cycles. The normal stress degradation is much greater at the invert location, and the majority of the normal stress degradation happens in the initial cycles. An increase in the soil overburden pressure and/or pipe weight further promotes this degradation which occurs in the first displacement cycle. This is due to the increase in confinement pressure and the tendency of the soil to contract during cyclic loading.

- Shear and normal stresses at different locations around the pipe and in different test scenarios follow complex paths. However, they all exhibit similar shear strength envelopes indicating that Coulomb friction theory holds for this problem.
- The maximum normal stress in each cycle at the invert location degrades with an increasing number of cycles. However, at the crown location, due to the low normal stress value and therefore localized dilation, it can experience an increase in the first cycle before subsequent degradation. At the springline location, the maximum normal stress increases in the first cycle; thereafter, it does not experience significant change with increasing number of cycles.
- The maximum shear resistance in each cycle also degrades during axial cyclic loading at the invert and crown locations. However, this degradation is insignificant at the pipe springlines. The rate of degradation reduces after the initial cycles before reaching a steady state. Increasing the surrounding soil relative density results in a considerable increase in the maximum shear resistance in each cycle.
- Using only a single set of input parameters, the proposed HWI approach was shown to provide a high-fidelity simulation of the complex soil-pipe interaction behaviour at the interface zones, including cyclic stress degradation, hardening, softening, cyclic accumulative contraction, reduction of stress degradation rate, steady sate/stabilization condition, and soil relative density effects. This numerical framework therefore provides an accurate and practical solution for soil-pipe interaction problems for a fraction of the computational cost of a three-dimensional finite element analysis.
- The proposed approach depends on the initial distribution of the normal stress around the pipe circumference, and the accuracy of this modeling approach in capturing the evolution of normal and shear stresses is increased if the initial distribution of normal stress is sufficiently accurate.

Acknowledgment

The authors acknowledges the support of the Natural Sciences and Engineering Research Council of Canada (NSERC) Grant no. RGPIN-2020-05515.

References

Ahmed, M.R., Tran, V.D.H., and Meguid, M.A. 2015. On the Role of Geogrid Reinforcement in Reducing Earth Pressure on Buried Pipes: Experimental and Numerical Investigations. Soils and Foundations, 55(3): 588–599. Japanese Geotechnical Society. doi:10.1016/j.sandf.2015.04.010.

Al-Khazaali, M., and Vanapalli, S.K. 2018. Axial force–displacement behaviour of a buried pipeline in saturated and unsaturated sand. Géotechnique, 69(11): 986–1003. ICE Publishing. doi:10.1680/jgeot.17.p.116.

ALA, A.L.A. 2001. Guidelines for the Design of Buried Steel Pipe. Washington, DC, USA.

ALA, A.L.A. 2005. Seismic Guidelines for Water Pipelines. Washington, DC, USA. Available from www.americanlifelinesalliance.org.

Anderson, C., Wijewickreme, D., Ventura, C., and Mitchell, A. 2004. Full-scale laboratory testing of buried polyethylene gas distribution pipelines subject to lateral ground displacements. *In* 13th World Conference on Earthquake Engineering. Vancouver, Canada. pp. 1–13.

Ansari, Y., Kouretzis, G., and Sloan, S.W. 2019. Physical modelling of lateral sand–pipe interaction. Géotechnique,: 1–16. Thomas Telford Ltd. doi:10.1680/jgeot.18.p.119.

Bilgin, Ö., Asce, M., and Stewart, H.E. 2009. Design Guidelines for Polyethylene Pipe Interface Shear Resistance. Journal of Geotechnical and Geoenvironmental Engineering, 135(6): 809–818. doi:10.1061/ASCEGT.1943-5606.0000030.

Bilgin, Ö., Asce, M., and Stewart, H.E. 2012. Studying Buried Pipeline Behavior Using Physical and Numerical Modeling. *In* GeoCongress 2012: state of the art and practice in geotechnical engineering. *Edited by* R.D. Hryciw and N. Athanasopoulos-Zekkos, Adda Yesiller. American Society of Civil Engineers, Oakland, California, United States. pp. 2128–2137. doi:https://doi.org/10.1061/9780784412121.218.

Bowles, J.E. 1996. Foundation analysis and design. McGraw-Hill.

Brennodden, by H., Sveggen, O., Wagner, D., and Murff, J. 1986. Full-Scale Pipe-Soil Interaction Tests. *In* Proceedings of the 18th annual offshore technology conference. pp. 433–440.

Bruton, D.A.S., Sinclair, F., and Carr -Atkins Boreas, M. 2010. Lessons Learned From Observing Walking of Pipelines with Lateral Buckles, Including New Driving Mechanisms and Updated Analysis Models. *In* Proceedings of the offshore technology conference. Offshore Technology Conference, Houston, Texas, USA. pp. 1–12.

Calvetti, F., di Prisco, C., and Nova, R. 2004. Experimental and numerical analysis of soil-pipe interaction. Journal of Geotechnical and Geoenvironmental Engineering, 130(12): 1292–1299. doi:10.1061/(ASCE)1090-0241(2004)130:12(1292).

Carr, M., Sinclair, F., Bruton, D., and Consultants, B. 2006. Pipeline Walking—Understanding the Field Layout Challenges, and Analytical Solutions Developed for the SAFEBUCK JIP. *In* Proceedings of Offshore Technology Conference. houston, Texas, USA. pp. 1–11.

Castelo, A., White, D., and Tian, Y. 2019. Simple solutions for downslope pipeline walking on elastic-perfectly-plastic soils. Ocean Engineering, 172: 671–683. Elsevier Ltd. doi:10.1016/j.oceaneng.2018.11.037.

Cheuk, C.Y., White, D.J., and Bolton, M.D. 2007. Large-scale modelling of soil-pipe interaction during large amplitude cyclic movements of partially embedded pipelines. Canadian Geotechnical Journal, 44(8): 977–996. doi:10.1139/T07-037.

Colliat, J.L., Desrues, J., and Flavigny, F. 1986. Avantages etinconvénients de l'utilisation d'un système d'antifrettage dansl'essai triaxial de compression. Revue Française de Géotechnique, 34: 41–55.

Dadfar, B., Hesham El Naggar, M., and Nastev, M. 2015. Ovalization of steel energy pipelines buried in saturated sands during ground deformations. Computers and Geotechnics, 69: 105–113. Elsevier Ltd. doi:10.1016/j.compgeo.2015.05.004.

Daiyan, N., Kenny, S., Phillips, R., and Popescu, R. 2011. Investigating pipeline-soil interaction under axial-lateral relative movements in sand. Canadian Geotechnical Journal, 48(11): 1683–1695. doi:10.1139/t11-061.

Dassault Systèmes. 2013. Abaqus Documentation.

DeJong, J.T., and Westgate, Z.J. 2009. Role of Initial State, Material Properties, and Confinement Condition on Local and Global Soil-Structure Interface Behavior. Journal of Geotechnical and Geoenvironmental Engineering, 135(11): 1646–1660. American Society of Civil Engineers. doi:10.1061/(ASCE)1090-0241(2009)135:11(1646).

Det Norske Veritas, D. 2007. Global buckling of submarine pipelines—Structural design due to high temperature/high pressure. Det Norske Veritas (DNV), Baerum, Norway. Available from http://webshop.dnv.com/global/,.

Dietz, M.S. 2000. Developing an holistic understanding of interface friction using sand within the direct shear apparatus.

Elshesheny, A., Mohamed, M., Nagy, N.M., and Sheehan, T. 2020. Numerical behaviour of buried flexible pipes in geogrid-reinforced soil under cyclic loading. Computers and Geotechnics, 122: 1–17, 103493. Elsevier Ltd. doi:10.1016/j.compgeo.2020.103493.

Elshesheny, A., Mohamed, M., and Sheehan, T. 2019a. Buried flexible pipes behaviour in unreinforced and reinforced soils under cyclic loading. Geosynthetics International, 26(2): 184–205. ICE Publishing. doi:10.1680/jgein.18.00046.

Elshesheny, A., Mohamed, M., and Sheehan, T. 2019b. Performance of buried rigid pipes under the application of incrementally increasing cyclic loading. Soil Dynamics and Earthquake Engineering, 125: 1–13, 105729. Elsevier Ltd. doi:10.1016/j.soildyn.2019.105729.

Fakharian, K. 1996. Three-dimensional monotonic and cyclic behaviour of sand-steel interfaces: Testing and modelling. Ph.D. thesis, University fo Ottowa, Ontario, Canada. Available from http://www.ruor.uottawa.ca/handle/10393/10238 [accessed 15 October 2015].

Flavigny, E., Desrues, J., and Palayer, B. 1990. Note technique:Le sable d'Hostun. Revue Française de Géotechnique, 53: 67–70.

Ghionna, V.N., and Mortara, G. 2002. An elastoplastic model for sand—structure interface behaviour. Géotechnique, 52(1): 41–50. doi:https://doi.org/10.1680/geot.2002.52.1.41.

Guha, I., White, D.J., and Randolph, M.F. 2019. Subsea pipeline walking with velocity dependent seabed friction. Applied Ocean Research, 82: 296–308. Elsevier Ltd. doi:10.1016/j.apor.2018.10.028.

Hammad, W.I. 1991. Modelisation nonlineaire etetude experimentale des bandes de cisaillement dans le sable. Universite Joseph Fourier, Grenoble, France.

Hill, A.., White, D.J., Bruton, D., Langford, T., Meyer, V., Jewell, R., and Ballard, J.-C. 2012. A new framework for axial pipe-soil interaction illustrated by a range of marine clay datasets. *In* Proceedings of international conference on offshore site investigation and geotechnics. Society of Underwater Technology, London, UK. pp. 367–377. Available from https://www.researchgate.net/publication/296492594.

Hu, L., and Pu, J. 2004. Testing and Modeling of Soil-Structure Interface. Journal of Geotechnical and Geoenvironmental Engineering, 130(8): 851–860. doi:10.1061/(ASCE)1090-0241(2004)130:8(851).

Huber, M., and Wijewickreme, D. 2014. Response of Buried District Heating Pipelines Under Relative Axial Movements. *In* Proceedings of the 10th international pipeline conference, IPC2014. ASME, Calgary, Alberta, Canada. pp. 1–5. Available from http://www.asme.org/about-asme/terms-of-use.

Karimian, S.A. 2006. Response of buried steel pipelines subjected to longitudinal and transverse ground movement. Ph.D. Thesis, Univeristy of British Columbia, Vancouver, Canada.

Lade, P. V., Yamamuro, J. a., and Bopp, P. a. 1996. Significance of Particle Crushing in Granular Materials. Journal of Geotechnical and Geoenvironmental Engineering, 122(4): 309–316.

doi:10.1061/(ASCE)1090-0241(1997)123:9(889).

Lee, D.H., Kim, B.H., Lee, H., and Kong, J.S. 2009. Seismic behavior of a buried gas pipeline under earthquake excitations. Engineering Structures, 31(5): 1011–1023. Elsevier. doi:10.1016/J.ENGSTRUCT.2008.12.012.

Low, H.E., Ramm, M., Bransby, M.F., White, D.J., and Westgate, Z.W. 2017. Effect of through-life changes in soil strength and axial pipe-seabed resistance for HPHT pipeline design. *In* International Conference on Offshore Site Investigation and Geotechnics. pp. 841–849. Available from https://www.researchgate.net/publication/327032638.

Martinez, A., Frost, J.D., and Hebeler, G.L. 2015. Experimental study of shear zones formed at sand/steel interfaces in axial and torsional axisymmetric tests. Geotechnical Testing Journal, 38(4): 409–426. ASTM International. doi:10.1520/GTJ20140266.

Martinez, A., Palumbo, S., and Todd, B.D. 2019. Bioinspiration for Anisotropic Load Transfer at Soil–Structure Interfaces. Journal of Geotechnical and Geoenvironmental Engineering, 145(10): 04019074. doi:10.1061/(asce)gt.1943-5606.0002138.

Meidani, M., Meguid, M.A., and Chouinard, L.E. 2017. Evaluation of Soil–Pipe Interaction under Relative Axial Ground Movement. Journal of Pipeline Systems Engineering and Practice, 8(4): 04017009. American Society of Civil Engineers (ASCE). doi:10.1061/(asce)ps.1949-1204.0000269.

Meidani, M., Meguid, M.A., and Chouinard, L.E. 2018. Estimating earth loads on buried pipes under axial loading condition: insights from 3D discrete element analysis. International Journal of Geo-Engineering, 9(1). Springer. doi:10.1186/s40703-018-0073-3.

Minh, N.H., and Zhang, D. 2019. Soil Responses to Monotonic and Cyclic Lateral Displacement of a Buried Pipe. Journal of Pipeline Systems Engineering and Practice, 10(3): 1-11,04019012. American Society of Civil Engineers (ASCE). doi:10.1061/(ASCE)PS.1949-1204.0000381.

Mir Mohammad Hosseini, S.., and Moghaddas Tafreshi, S.N. 2002. Soil-Structure Interaction of Buried Pipes Under Cyclic Loading Conditions. International Journal of Engineering-Transactions B: Applications, 15(2): 117–124.

Mujtaba, H., Farooq, K., Sivakugan, N., and Das, B.M. 2018. Evaluation of relative density and friction angle based on SPT-N values. KSCE Journal of Civil Engineering, 22(2): 572–581. Springer Verlag. doi:10.1007/s12205-017-1899-5.

O'Hara, K.B., and Martinez, A. 2020. Monotonic and Cyclic Frictional Resistance Directionality in Snakeskin-Inspired Surfaces and Piles. Journal of Geotechnical and Geoenvironmental Engineering, 146(11): 04020116. American Society of Civil Engineers (ASCE). doi:10.1061/(asce)gt.1943-5606.0002368.

Orourke, M.J., and Hmadi, K. El. 1988. ANALYSIS OF CONTINUOUS BURIED PIPELINES FOR SEISMIC WAVE EFFECTS. EARTHQUAKE ENGINEERING AND STRUCTURAL DYNAMICS, 16: 917–929.

Palmer, A., Palmer, A., Ellinas, C., Richards, D., Register, Y., Guijt, J., and Norske Shell, A. 1990. Design of Submarine Pipelines Against Upheaval Buckling. *In* 22nd Annual OTC. Offshore Technology Conference, Houston, Texas. p. 551.

Pra-Ai, S. 2013. Behaviour of interfaces subjected to a large number of cycles. Application to piles. Ph.D. Thesis, Universite De Grenoble, France.

Di Prisco, C., and Galli, A. 2006. Soil-pipe interaction under monotonic and cyclic loads: experimental and numerical modelling. *In* 1st Euro Mediterranean Symposium on "Advances in Geomaterials and Structures". Hammamet, Tunisia. pp. 755–760.

Psyrras, N., Kwon, O., Gerasimidis, S., and Sextos, A. 2019. Can a buried gas pipeline experience local buckling during earthquake ground shaking? Soil Dynamics and Earthquake Engineering, 116: 511–529. Elsevier Ltd. doi:10.1016/j.soildyn.2018.10.027.

Psyrras, N.K., and Sextos, A.G. 2018. Safety of buried steel natural gas pipelines under earthquake-induced ground shaking: A review. Soil Dynamics and Earthquake Engineering, 106: 254–277. Elsevier Ltd. doi:10.1016/j.soildyn.2017.12.020.

Rajeev, P., and Kodikara, J. 2011. Numerical analysis of an experimental pipe buried in swelling soil.

Computers and Geotechnics, 38(7): 897–904. doi:10.1016/j.compgeo.2011.06.005.

Randolph, M.F. 2012. Cyclic Interface Shearing in Sand and Cemented Soils and Application to Axial Response of Piles. *In* Mechanical Behaviour of Soils Under Environmentally Induced Cyclic Loads. *Edited by* Di Prisco C. and Wood D.M. Springer, Vienna. pp. 481–528. doi:https://doi.org/10.1007/978-3-7091-1068-3_10.

Randolph, M.F., White, D.J., and Yan, Y. 2012. Modelling the axial soil resistance on deep-water pipelines. Geotechnique, 62(9): 837–846. doi:10.1680/geot.12.OG.010.

Reda, A., Sultan, I.A., Howard, I.M., Forbes, G.L., and McKee, K.K. 2018. Pipeline walking and anchoring considerations in the presence of riser motion and inclined seabed. International Journal of Pressure Vessels and Piping, 162: 71–85. Elsevier Ltd. doi:10.1016/j.ijpvp.2018.01.003.

Rui, S., Wang, L., Guo, Z., Cheng, X., and Wu, B. 2021. Monotonic behavior of interface shear between carbonate sands and steel. Acta Geotechnica, 16: pages167–187. Springer. doi:10.1007/s11440-020-00987-9.

Saberi, M., Annan, C.-D., and Konrad, J.-M. 2017. Constitutive Modeling of Gravelly Soil-Structure Interface Considering Particle Breakage. Journal of Engineering Mechanics, 143(8): 04017044 (14 pp.). doi:10.1061/(ASCE)EM.1943-7889.0001246.

Saberi, M., Annan, C.-D., and Konrad, J.-M. 2018a. A Unified Constitutive Model for Simulating Stress-Path Dependency of Sandy and Gravelly Soil-Structure interfaces. International Journal of Non-Linear Mechanics, 102: 1–13. doi:10.1016/j.ijnonlinmec.2018.03.001.

Saberi, M., Annan, C.-D., and Konrad, J.-M. 2018b. On the mechanics and modeling of interfaces between granular soils and structural materials. Archives of Civil and Mechanical Engineering, 18(4): 1562–1579. Politechnika Wrocławska. doi:https://doi.org/10.1016/j.acme.2018.06.003.

Saberi, M., Annan, C.-D., and Konrad, J.-M. 2020a. A non-linear interface model for monotonic shear coupling in granular soil-structure interaction problems. Géotechnique Letters, 10(2): 336–345. doi:10.1680/jgele.19.00041.

Saberi, M., Annan, C.-D., Konrad, J.-M., and Lashkari, A. 2016. A critical state two-surface plasticity model for gravelly soil-structure interfaces under monotonic and cyclic loading. Computers and Geotechnics, 80: 71–82. doi:10.1016/j.compgeo.2016.06.011.

Saberi, M., Annan, C.D., and Konrad, J.M. 2019. Implementation of a soil-structure interface constitutive model for application in geo-structures. Soil Dynamics and Earthquake Engineering, 116: 714–731. doi:10.1016/j.soildyn.2018.11.001.

Saberi, M., Annan, C.D., and Konrad, J.M. 2020b. Three-dimensional constitutive model for cyclic behavior of soil-structure interfaces. Soil Dynamics and Earthquake Engineering, 134: 106162 (1–15). Elsevier Ltd. doi:10.1016/j.soildyn.2020.106162.

Saberi, M., Arabzadeh, H., and Keshavarz, A. 2011a. Numerical analysis of buried pipelines with right angle elbow under wave propagation. Procedia Engineering, 14: 3260–3267. doi:10.1016/j.proeng.2011.07.412.

Saberi, M., Behnamfar, F., and Vafaeian, M. 2013. A semi-analytical model for estimating seismic behavior of buried steel pipes at bend point under propagating waves. Bulletin of Earthquake Engineering, 11(5): 1373–1402. doi:10.1007/s10518-013-9430-y.

Saberi, M., Behnamfar, F., and Vafaeian, M. 2015. A Continuum Shell-beam Finite Element Modeling of Buried Pipes with 90-degree Elbow Subjected to Earthquake Excitations. International Journal of Engineering - Transactions C: Aspects, 28(3): 338–349. doi:10.5829/idosi.ije.2015.28.03c.02.

Saberi, M., Halabian, A.M., and Vafaian, M. 2011b. Numerical analysis of buried steel pipelines under earthquake excitations. *In* Pan-Am CGS Geotechnical Conference. Canadian Society of Civil Engineering, Toronto, Canada. pp. 1–7. Available from https://www.researchgate.net/publication/329266601.

Sarvanis, G.C., Karamanos, S.A., Vazouras, P., Mecozzi, E., Lucci, A., and Dakoulas, P. 2018. Permanent earthquake-induced actions in buried pipelines: Numerical modeling and experimental verification. Earthquake Engineering and Structural Dynamics, 47(4): 966–987. John Wiley and Sons Ltd. doi:10.1002/eqe.3001.

Scarpelli, G., Sakellariadi, E., Furlani, G., and Associato Sintesi, S. 2003. Evaluation of soil-pipeline longitudinal interaction forces. Rivista Italiana di Geotecnica, 4(3): 24–41. Available from https://www.researchgate.net/publication/334680603.

Shahrour, I., and Rezaie, F. 1997. An elastoplastic constitutive relation for the soil-structure interface under cyclic loading. Computers and Geotechnics, 21(1): 21–39. doi:10.1016/S0266-352X(97)00001-3.

Sheil, B.B., Martin, C.M., and Byrne, B.W. 2021. Simulation of overburden pressure during laboratory investigations of axial pipe-soil interaction. Géotechnique, 71(3): 272–278. doi:https://doi.org/10.1680/jgeot.18.T.040.

Sheil, B.B., Martin, C.M., Byrne, B.W., Plant, M., Williams, K., and Coyne, D. 2018. Full-scale laboratory testing of a buried pipeline in sand subjected to cyclic axial displacements. Géotechnique, 68(8): 684–698. ICE Publishing. doi:10.1680/jgeot.16.P.275.

Takada, S., and Tanabe, K. 1987. Three-Dimensional Seismic Response Analysis of Buried Continuous or Jointed Pipelines. Journal of Pressure Vessel Technology , 109(1): 80–87. Available from http://www.asme.org/about-asme/terms-of-use.

Talesnick, M.L., Xia, H.W., and Moore, I.D. 2011. Earth pressure measurements on buried HDPE pipe. Geotechnique, 61(9): 721–732. doi:10.1680/geot.8.P.048.

Tian, Y., Cassidy, M.J., and Gaudin, C. 2010. Advancing pipe-soil interaction models in calcareous sand. Applied Ocean Research, 32(3): 284–297. doi:10.1016/j.apor.2010.06.002.

Tian, Y., Wu, W., Cassidy, M.J., and Randolph, M.F. 2021. A complete analytical solution for axial pipeline walking considering seabed resistance as rigid plastic behaviour. Géotechnique,: 1–15. Thomas Telford Ltd. doi:10.1680/jgeot.20.p.135.

Tsinidis, G., Di Sarno, L., Sextos, A., and Furtner, P. 2019. A critical review on the vulnerability assessment of natural gas pipelines subjected to seismic wave propagation. Part 2: Pipe analysis aspects. Tunnelling and Underground Space Technology, 92: 103056 (1–19). Elsevier BV. doi:10.1016/j.tust.2019.103056.

Tsinidis, G., Di Sarno, L., Sextos, A., and Furtner, P. 2020. Optimal intensity measures for the structural assessment of buried steel natural gas pipelines due to seismically-induced axial compression at geotechnical discontinuities. Soil Dynamics and Earthquake Engineering, 131: 106030 (1–22). Elsevier Ltd. doi:10.1016/j.soildyn.2019.106030.

Vafaei, N., Fakharian, K., and Sadrekarimi, A. 2019. An Experimental Study on Effect of Boundary Condition on Particle Damage in Shear Zone of Crushed Sand. Journal of Geophysical Research: Solid Earth, 124(9): 9546–9561. Blackwell Publishing Ltd. doi:10.1029/2018JB017153.

Vafaei, N., Fakharian, K., and Sadrekarimi, A. 2021. Sand-sand and sand-steel interface grain-scale behavior under shearing. Transportation Geotechnics, 30. Elsevier Ltd. doi:10.1016/j.trgeo.2021.100636.

Vangla, P., and Latha Gali, M. 2016. Effect of particle size of sand and surface asperities of reinforcement on their interface shear behaviour. Geotextiles and Geomembranes, 44(3): 254–268. Elsevier Ltd. doi:10.1016/j.geotexmem.2015.11.002.

Vazouras, P., Dakoulas, P., and Karamanos, S.A. 2015. Pipe-soil interaction and pipeline performance under strike-slip fault movements. Soil Dynamics and Earthquake Engineering, 72: 48–65. Elsevier Ltd. doi:10.1016/j.soildyn.2015.01.014.

Vazouras, P., Karamanos, S.A., and Dakoulas, P. 2010. Finite element analysis of buried steel pipelines under strike-slip fault displacements. Soil Dynamics and Earthquake Engineering, 30(11): 1361–1376. doi:10.1016/j.soildyn.2010.06.011.

Weidlich, I., and Achmus, M. 2006. Reduction of friction forces between soil and buried district heating pipes due to cyclic axial displacements. *In* Proceedings ofthe 10th international symposium on district heating and cooling. Gothenburg, Sweden. pp. 18–27. Available from http://www.unics.uni-hannover.de/nhgwigbe/.

Weidlich, I., and Achmus, M. 2008. Measurement of Normal Pressures and Friction Forces Acting on Buried Pipes Subjected to Cyclic Axial Displacements in Laboratory Experiments. Geotechnical Testing Journal, 31(4): 334–343. doi:https://doi.org/10.1520/GTJ100804.

White, D., Bruton, D.A.S., Bolton, M., Hill, A.J., Ballard, J.-C., and Langford, T. 2011. SAFEBUCK

JIP - Observations of Axial Pipe-soil Interaction from Testing on Soft Natural Clays. *In* Proceedings of offshore technology conference. offshore technology conference, Houston, USA. pp. 1–29. doi:10.4043/21249-ms.

Wijewickreme, D., Karimian, H., and Honegger, D. 2009. Response of buried steel pipelines subjected to relative axial soil movement. Canadian Geotechnical Journal, 46(7): 735–752. Canadian Science Publishing. doi:10.1139/t09-019.

Xie, X., Symans, M.D., O'Rourke, M.J., Abdoun, T.H., O'Rourke, T.D., Palmer, M.C., and Stewart, H.E. 2013. Numerical modeling of buried HDPE pipelines subjected to normal faulting: A case study. Earthquake Spectra, 29(2): 609–632. doi:10.1193/1.4000137.

Yang, R., Kameda, H., and Takada, S. 1988. Shell Model FEM Analysis of Buried Pipelines under Seismic Loading. Bulletin of the Disaster Prevention Research Institute, 38(3): 115–146.

Zhang, G., and Zhang, J.-M. 2009. Constitutive rules of cyclic behavior of interface between structure and gravelly soil. Mechanics of Materials, 41(1): 48–59. Elsevier Ltd. doi:10.1016/j.mechmat.2008.08.003.

Zhang, J., Stewart, D.P., and Randolph, M.F. 2001. Centrifuge modelling of drained behaviour for pipelines shallowly embedded in calcareous sand. International Journal of Physical Modelling in Geotechnics, 1(1): 25–39.

Zhang, J., Stewart, D.P., and Randolph, M.F. 2002. Kinematic Hardening Model for Pipeline-Soil Interaction under Various Loading Conditions. International Journal of Geomechanics, 2(4): 419–446. American Society of Civil Engineers (ASCE). doi:10.1061/(asce)1532-3641(2002)2:4(419).

List of Tables

Table 1 Properties of sandy soils used in laboratory tests

Table 2 Parameters for determination of N_{ch} and N_{qh} (ALA 2001)

Table 3 Constitutive equations of the interface model and model parameters

Table 4 Calibrated parameters for the interface constitutive model

Table 5 Input parameters for soil spring force-displacement relationships

Figures Captions

Figure 1. Soil-pipe interaction modelling approaches; a) Beam-on-nonlinear-Winkler-foundation, b) Shell on Winkler foundation, and C) Hybrid beam-shell model.

Figure 2. Front and side views of test set-up showing instrumented test pipe installed in a tank

Figure 3. Schematic of soil-pipe interaction testing scenarios, a) scenario I, b) scenario II, and c) scenario III

Figure 4. Salient locations around the pipe circumference

Figure 5. Proposed modeling approach for soil-pipe interaction analysis at the pipe a) crown, b) springlines, and c) invert.

Figure 6. Illustration of the calibration process for interface model parameters of D_{t0}, μ^{cs}, $e_{cs\text{-}0}$, and λ for Hostun sand (Sheil et al. 2018). See Table 3 for description of parameters.

Figure 7. Representation for calibration of the interface model parameter k^f for Hostun sand by Sheil et al. (2018).

Figure 8. Calibration of model predictions using experimental measurements of local normal contact stresses for Hostun sand for test scenario II (Sheil et al. (2018)); a) measured σ_n-Δ, and b) predicted σ_n-Δ.

Figure 9. Sensitivity analysis on the interface constitutive model parameters K^d and A^d

Figure 10. Calibration of model predictions using experimental measurements of local shear contact stresses for Hostun sand for test scenario II (Sheil et al. 2018); a) measured τ-Δ, and b) predicted τ-Δ.

Figure 11. Representation for calibration of particle breakage parameters b_{r1} and b_{r2} of the interface model for Hostun sand (Sheil et al. 2018).

Figure 12. Calibration of model predictions using experimental measurements for quartz sand-HDPE pipe system (Weidlich and Achmus 2006, 2008); a) F-Δ with h/D = 1.5 and D_r=0.7, and b) pipe settlement-N with h/D = 3 and D_r=0.4.

Figure 14. Comparison between model predictions and experimental measurements of contact stress development during cyclic loading for test scenario I, a) measured τ-N, b) measured σ_n-N, c) predicted τ-N, and d) predicted σ_n-N.

Figure 13. Comparison between model predictions and experimental measurements for sand-HDPE pipe system by Bilgin et al.(2009) used for model calibration.

Figure 15. Local contact stress paths at the crown, invert and springline locations for test scenario I, a) laboratory measurements, and b) numerical predictions.

Figure 16. Comparison between model predictions and experimental measurements of contact stress development during cyclic loading for test scenario II, a) measured τ-N, b) measured σ_n-N, c) predicted τ-N, and d) predicted σ_n-N.

Figure 17. Local contact stress paths at the crown, invert and springline locations for test scenario II, a) laboratory measurements, and b) numerical predictions.

Figure 18. Comparison between model predictions and experimental measurements of contact stress development during cyclic loading for test scenario III, a) measured τ-N, b) measured σ_n-N, c) predicted τ-N, and d) predicted σ_n-N.

Figure 19. Local contact stress paths at the crown, invert and springline locations for test scenario III, a) laboratory measurements, and b) numerical predictions.

Figure 20. Experimental and numerical modeling comparisons for pipe settlement for all three test scenarios, a) laboratory measurements, and b) numerical predictions.

Figure 21. Maximum contact stress variation during cyclic loading at pipe crown; a) $\sigma_{n\text{-}max}$, scenario I, test, b) $\sigma_{n\text{-}max}$, scenario II, c) $\sigma_{n\text{-}max}$, scenario III, d) τ_{max}, scenario I, e) τ_{max}, scenario II, and f) τ_{max}, scenario III.

Figure 22. Maximum contact stress variation during cyclic loading at pipe invert; a) $\sigma_{n\text{-}max}$, scenario I, test, b) $\sigma_{n\text{-}max}$, scenario II, c) $\sigma_{n\text{-}max}$, scenario III, d) τ_{max}, scenario I, e) τ_{max}, scenario II, and f) τ_{max}, scenario III.

Figure 23. Maximum contact stress variation during cyclic loading at pipe springline; a) $\sigma_{n\text{-}max}$, scenario I, test, b) $\sigma_{n\text{-}max}$, scenario II, c) $\sigma_{n\text{-}max}$, scenario III, d) τ_{max}, scenario I, e) τ_{max}, scenario II, and f) τ_{max}, scenario III.

Figure 24. Comparison between model predictions and experimental measurements for quartz sand-HDPE pipe system (Weidlich and Achmus 2006, 2008); F-Δ with h/D=1.5 and D_r =0.7.

Figure 25. Comparison between model predictions and experimental measurements for quartz sand-HDPE pipe system (Weidlich and Achmus 2006, 2008); F_{max}-N with h/D=3 and D_r =0.4, 0.5 and 0.7.

Figure 26. Comparison between model predictions and experimental measurements for sand-HDPE pipe system (Bilgin et al. 2009) in τ-Δ plane; a) test, and b) model.

Figure 27. Comparison between model predictions and laboratory testing for τ_{max} against N for buried HDPE pipe (Bilgin et al. 2009).